



Calhoun: The NPS Institutional Archive
DSpace Repository

Theses and Dissertations

1. Thesis and Dissertation Collection, all items

1994-03

Development of an experimental facility for analysis of rotordynamic phenomena

Simei, Frank A.

Monterey, California. Naval Postgraduate School

<http://hdl.handle.net/10945/28120>

Downloaded from NPS Archive: Calhoun



<http://www.nps.edu/library>

Calhoun is the Naval Postgraduate School's public access digital repository for research materials and institutional publications created by the NPS community. Calhoun is named for Professor of Mathematics Guy K. Calhoun, NPS's first appointed -- and published -- scholarly author.

Dudley Knox Library / Naval Postgraduate School
411 Dyer Road / 1 University Circle
Monterey, California USA 93943

DUDLEY KNOX LIBRARY
NAVAL POSTGRADUATE SCHOOL
MONTEREY CA 93543-5101

Approved for public release; distribution is unlimited

**Development of an Experimental Facility
for Analysis of Rotordynamic Phenomena**

by

Frank A. Sime, Jr.
Lieutenant, United States Navy
B.S., United States Naval Academy, 1985

Submitted in partial fulfillment of
requirements for the degree of

MASTER OF SCIENCE IN MECHANICAL ENGINEERING

from the

NAVAL POSTGRADUATE SCHOOL
March 1994

Unclassified

Security Classification of this page

REPORTS DOCUMENTATION PAGE

1a Report Security Classification Unclassified		1b Restrictive Markings	
2a Security Classification Authority		3 Distribution Availability of Report Approved for public release; distribution unlimited	
2b Declassification/Downgrading Schedule		5 Monitoring Organization Report Number(s)	
6a Name of Performing Organization Naval Postgraduate School	6b Office Symbol (If Applicable) ME	7a Name of Monitoring Organization	
6c Address (city, state, and ZIP code) Monterey, CA 93940-5000		7b Address (city, state, and ZIP code)	
8a Name of Funding/ Sponsoring Organization	8b Office Symbol (If Applicable)	9 Procurement Instrument Identification Number	
8c Address (city, state, and ZIP code)		10 Source of Funding Numbers	
Program Element Number	Project No.	Task	Work Unit Accession No.
11 Title (Include Security Classification) Development of an Experimental Facility for Analysis of Rotordynamic Phenomena			
12 Personal Author(s) Frank A. Simej, Jr.			
13a Type of Report Master of Science Thesis	13b Time Covered From To	14 Date of Report (year, month, day) March 1994	15 Page count 71
16 Supplementary Notation			
17 Cosati Codes:	Field	Group	Subgroup
18 Subject Terms (continue on reverse if necessary and identify by block number) Bentley Nevada Rotor Kit, LabVIEW Virtual Instrument, Rotordynamic Characteristics, Cascade Plots, Synchronous Whirl, Backward W			
19 Abstract (continue on reverse if necessary and identify by block number) An experimental facility was developed to investigate the rotordynamic phenomena of rotating machinery during subcritical, resonant and supercritical operation. The facility consists of a Bentley Nevada Corporation Rotor Kit integrated with a computerized data acquisition and control process. A LabVIEW Virtual Instrument was designed to collect, analyze and display rotor position and rotor displacement information. Experiments conducted included construction of Cascade plots, analytic prediction of the first lateral mode and demonstration of synchronous whirl due to a mass imbalance; during which, backward whirl was experienced. The behavior of the rotor was characterized throughout the operating range.			
20 Distribution/Availability of Abstract X unclassified/unlimited same as report DTIC users		21 Abstract Security Classification Unclassified	
22a Name of Responsible Individual Professor Knox T. Millsaps, Jr.		22b Telephone (Include Area Code) (408) 656-3382	22c Office Symbol ME-MI

DD FORM 1473, 84 MAR

83 APR edition may be used until exhausted security classification of this
All other editions are obsolete Unclassified

ABSTRACT

An experimental facility was developed to investigate the rotordynamic phenomena of rotating machinery during subcritical, resonant and supercritical operation. The behavior of the rotor was characterized throughout the operating range. The facility consists of a Bentley Nevada Corporation Rotor Kit integrated with a computerized data acquisition and control process. A LabVIEW Virtual Instrument was designed to collect, analyze and display rotor position and rotor displacement information. Experiments conducted included construction of Cascade plots, analytic prediction of the first lateral mode and demonstration of synchronous whirl due to a mass imbalance; during which, backward whirl was experienced.

TABLE OF CONTENTS

I. INTRODUCTION	1
II. EXPERIMENTAL FACILITY GENERAL DESCRIPTION.....	4
A. EXPERIMENTAL FACILITY HARDWARE	4
B. EXPERIMENTAL FACILITY SOFTWARE	11
III. ROTOR CHARACTERISTICS: CASCADE PLOTS.....	13
A. ROTOR ASSEMBLY CONFIGURATION	13
B. DISCUSSION OF THE RESULTS.....	14
1. Rotor disk at $a=8.5$ inches: Centered	14
2. Rotor disk at $a=4.25$ inches: $1/4$ Axial.....	15
3. Rotor disk at $a=2.125$ inches: $1/8$ Axial.....	15
IV. ANALYTICAL PREDICTION OF THE FIRST LATERAL MODE.....	20
A. ROTOR ASSEMBLY CONFIGURATION	20
B. THEORETICAL UPPER BOUND: RAYLEIGH'S METHOD.....	20
C. THEORETICAL LOWER BOUND: DUNKERLEY'S FORMULA	23
D. DISCUSSION OF THE RESULTS.....	24
V. SYNCHRONOUS WHIRL DUE TO A MASS IMBALANCE.....	27
A. THEORETICAL BACKGROUND: SYNCHRONOUS WHIRL	27
B. ROTOR ASSEMBLY CONFIGURATION	30
C. DISCUSSION OF THE RESULTS.....	31
1. Maximum Rotor Displacement Versus Rotor Speed.....	31

2. Rotor Orbits Characteristics..... 34

3. Maximum Y-Displacement - Mass Imbalance Phase Shift 36

D. BACKWARD WHIRL..... 36

VI. CONCLUSIONS AND RECOMMENDATIONS 43

 A. CONCLUSIONS 43

 B. RECOMMENDATIONS..... 45

APPENDIX A: LIST OF DIMENSIONS AND PROPERTIES 46

APPENDIX B: PROXIMETER CALIBRATION CURVE 47

APPENDIX C: PROXIMETER CONFIGURATION 48

APPENDIX D: NI AT-MIO-16F-5 CONFIGURATION..... 50

APPENDIX E: ROTOR.VI VIRTUAL INSTRUMENT 51

APPENDIX F: SYNCHRONOUS WHIRL TEST MATRIX..... 58

LIST OF REFERENCES..... 59

INITIAL DISTRIBUTION LIST..... 60

LIST OF FIGURES

Figure 1.	Photograph of the Experimental Facility.....	5
Figure 2.	Photograph of the Benley Nevada Rotor Assembly in a Simply Supported, Single Rotor Disk Configuration.....	5
Figure 3.	Block Diagram of the Experimental Facility.....	6
Figure 4.	Benley Nevada Rotor Assembly Diagram.	8
Figure 5.	Time Trace for the Y-Displacement for a Rotor Speed of 5560 RPM. Rotor Assembly in a Simply Supported, Single Disk Configuration, Rotor Length of 17.0 Inches, Disk Located 8.5 Inches from the Inboard Bearing Support with a 2 Gram Mass Imbalance.	16
Figure 6.	The Power Spectral Density Plot of the Y-Displacement Time Trace Shown Above in Figure (5).	16
Figure 7.	Cascade Plots of the Rotor Assembly in a Simply Supported, Single Disk Configuration, Rotor Length of 17.0 Inches, Disk Located 8.5 Inches from the Inboard Bearing Support with a 2 Gram Mass Imbalance.	17
Figure 8.	Cascade Plots of the Rotor Assembly in a Simply Supported, Single Disk Configuration, Rotor Length of 17.0 Inches, Disk Located 4.25 Inches from the Inboard Bearing Support with a 2 Gram Mass Imbalance.	18
Figure 9.	Cascade Plots of the Rotor Assembly in a Simply Supported, Single Disk Configuration, Rotor Length of 17.0 Inches, Disk Located 2.125 Inches from the Inboard Bearing Support with a 2 Gram Mass Imbalance.	19
Figure 10.	Rotor Assembly Model.....	21
Figure 11.	Theoretical and Experimental First Lateral Natural Frequency as a Function of Rotor Disk Position. The Rotor Assembly is in a Simply Supported, Single Disk Configuration, Rotor Length of 14.5 Inches, Disk with a Two Gram Mass Imbalance.	26
Figure 12.	Synchronous Whirl and Synchronous Whirl Orbit.....	28
Figure 13.	Theoretical Plots of the Whirl Radius (R) and the Maximum Displacement-Mass Imbalance Phase Lag (l) Versus Rotor Speed for a System with Slight Damping.....	29
Figure 14.	Experimental Results of the Maximum Y-Displacement Versus Rotor Speed. The Rotor Assembly is in a Simply Supported, Single Disk Configuration, Rotor Length of 14.5 Inches, Disk Located 7.25 Inches from the Inboard Bearing Support (Centered) with a 1.6 Gram Mass Imbalance.....	32

Figure 15.	Experimental Results of the Whirl Orbit Major Radius (R), Maximum Y-Displacement and Maximum X-Displacement Versus Rotor Speed. The Rotor Assembly is in a Simply Supported, Single Disk Configuration, Rotor Length of 14.5 Inches, Disk Located 7.25 Inches from the Inboard Bearing Support (Centered) with a 1.6 Gram Mass Imbalance.....	33
Figure 16.	Rotor Orbits for Speeds Subcritical Speeds of 1809 - 2465 - 2556 - 2616 - 2675 - 2715 RPM. The Rotor is Experiencing Forward Whirl. The Rotor Assembly is in a Simply Supported, Single Disk Configuration, Rotor Length of 14.5 Inches, Disk Located 7.25 Inches from the Inboard Bearing Support (Centered) with a 1.6 Gram Mass Imbalance.....	37
Figure 17.	Rotor Orbit for the First Critical Speed 2740 RPM. The Rotor is Experiencing Forward Whirl. The Rotor Assembly is in a Simply Supported, Single Disk Configuration, Rotor Length of 14.5 Inches, Disk Located 7.25 Inches from the Inboard Bearing Support (Centered) with a 1.6 Gram Mass Imbalance.....	38
Figure 18.	Rotor Orbits for Supercritical Speeds of 2760 - 2784 - 2809 - 2840 - 2898 RPM. The Rotor is Experiencing Backward Whirl. The Rotor Assembly is in a Simply Supported, Single Disk Configuration, Rotor Length of 14.5 Inches, Disk Located 7.25 Inches from the Inboard Bearing Support (Centered) with a 1.6 Gram Mass Imbalance.....	39
Figure 19.	Rotor Orbits for Supercritical Speeds of 2952 - 3022 - 3189 - 3501 - 4104 - 4603 RPM. The Rotor is Experiencing Forward Whirl. The Rotor Assembly is in a Simply Supported, Single Disk Configuration, Rotor Length of 14.5 Inches, Disk Located 7.25 Inches from the Inboard Bearing Support (Centered) with a 1.6 Gram Mass Imbalance.....	40
Figure 20.	Rotor Orbit for Supercritical Speed of 5560 RPM. The Rotor is Experiencing Synchronous and Subsynchronous Forward Whirl. The Rotor Assembly is in a Simply Supported, Single Disk Configuration, Rotor Length of 14.5 Inches, Disk Located 7.25 Inches from the Inboard Bearing Support (Centered) with a 1.6 Gram Mass Imbalance.....	41
Figure 21.	Maximum Y-Displacement - Mass Imbalance Phase Shift Versus Rotor Speed. The Rotor Assembly is in a Simply Supported, Single Disk Configuration, Rotor Length of 14.5 Inches, Disk Located 7.25 Inches from the Inboard Bearing Support (Centered) with a 1.6 Gram Mass Imbalance.....	42
Figure 22.	Eddy Current Proximeter Calibration Curve.....	47
Figure 23.	ROTOR.VI Front Panel.....	55
Figure 24.	ROTOR.VI Block Diagram.....	56
Figure 25.	ROTOR.VI Hierarchy.....	57

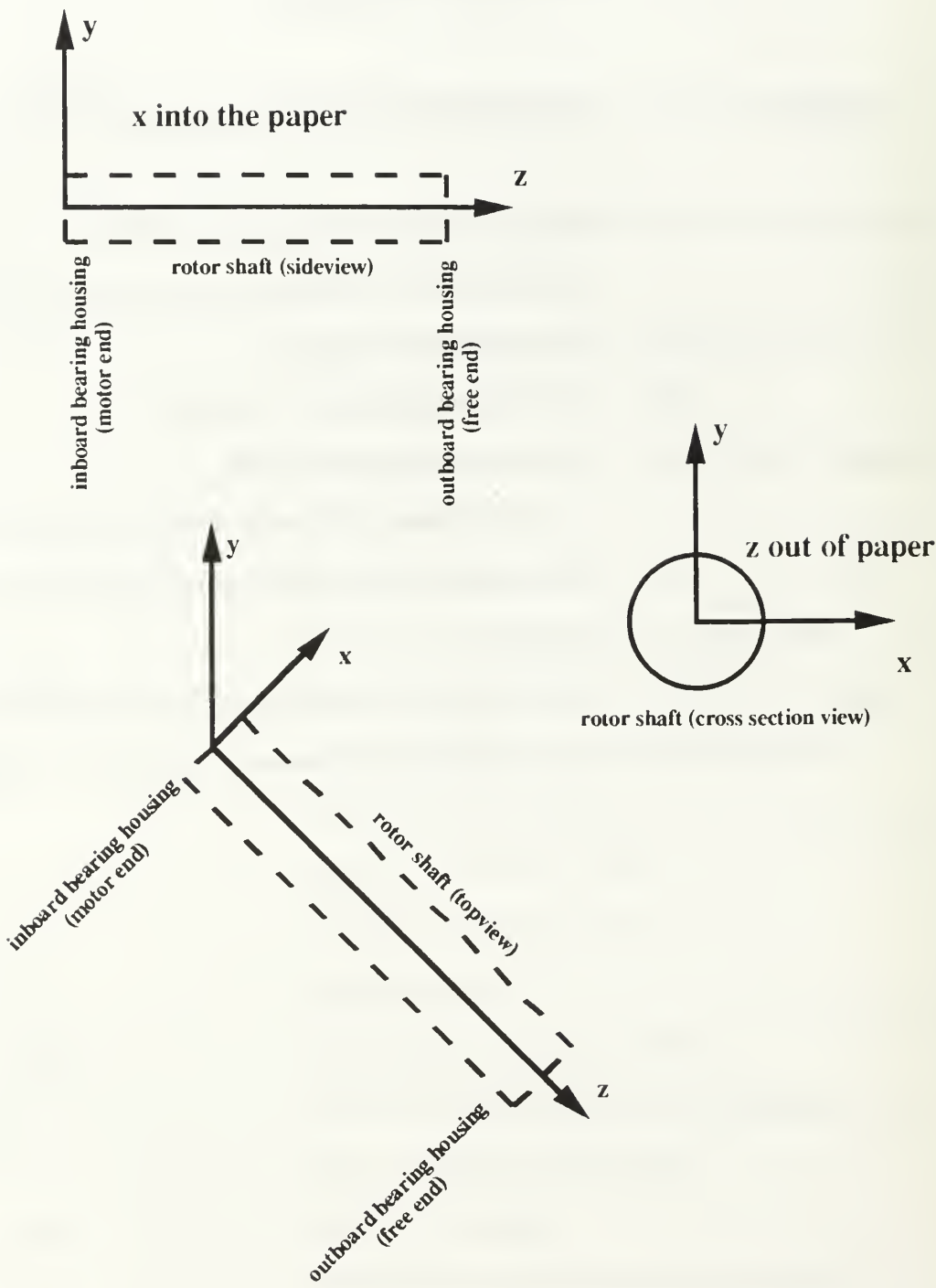
NOMENCLATURE

<u>SYMBOL</u>	<u>DEFINITION (units, U.S. Customary)</u>
a	Distance of the rotor disk's centerline from the inboard bearing support. (in)
a ₂₂	Influence coefficient due to an unit load applied at the location of the rotor disk. (in/lbf)
b	Distance of the rotor disk's centerline from the outboard bearing support. (in)
d	Diameter of the rotor shaft. (in)
E	Modulus of elasticity of the rotor shaft. (psi)
FFT	Discrete Fourier Transform. (mils sec)
I	First moment of inertia of the rotor shaft. (in ⁴)
L	Length of the rotor shaft. (in)
m	Mass of the rotor disk. (lbm)
M	Mass of the rotor shaft. (lbm)
N	Number of scans.
PSD	Power spectral density. (mils/HZ)
q	Center of mass offset due to a mass imbalance. (in)
R	Whirl orbit major radius. (mils)
x,y,z	Cartesian coordinates.
y(z)	Shape function as a function of axial position. (in)

GREEK SYMBOLS

<u>SYMBOL</u>	<u>DEFINITION (units, U.S. Customary)</u>
γ	Weight density of the rotor shaft. (lbf/in ³)
λ	Phase lag between the maximum rotor displacement and the mass imbalance. (degrees)
ρ	Density of the rotor shaft. (lbm/in ³)
ω	Rotor rotational speed. (RPM)
ω_n	First lateral natural frequency of the rotor assembly. (RPM)
ω_{11}	First lateral natural frequency of the rotor shaft only. (RPM)
ω_{22}	First lateral natural frequency of the rotor mass mounted on the rotor shaft in the absence of other masses. (RPM)

COORDINATE SYSTEM



I. INTRODUCTION

Rotordynamics is a continuously growing field, essential for the design of safe, reliable machinery. As the demand for higher power, higher performance machinery increases, the need to accurately predict and analyze the dynamic response of rotating shafts becomes increasingly important.

The many uses of rotating shafts includes many industrial, space and military applications. Examples of such use are steam and gas propulsion turbines, turbine generators, power-transmission shafting, pumps and compressors. These machines operate through conditions of varying speeds and loads. As technology advances, these machines are becoming lighter in weight, higher in speed, and more power dense machines, making the shaft more flexible. Thus, making understanding of the various complex rotordynamic phenomena which occur more important.

Inherent to rotating shafts are numerous rotordynamic phenomena associated with radial or lateral, torsional and longitudinal vibrations. The list of rotordynamic phenomena is extensive. Several examples include resonances at critical speeds, synchronous shaft whirl, chatter and rotordynamic instabilities. The causes of the different rotordynamic phenomena easily outnumber the types of phenomena, examples of which are residual rotor unbalance, shaft bow, rub conditions, bearing support asymmetry and coupling, and oil whirl conditions. It is the accurate analytical modeling of such complex conditions which challenge the designer.

In the past, the most extensive portion of the literature on the dynamics of rotating shafts was concerned with determining critical speeds and natural frequencies. It followed that most rotating machinery had been designed to operate below the first critical speed

which usually assured safe, reliable operation. However, most modern rotating machinery operate at speeds greater than the first critical speed. Designers now face a larger, more complex scope of rotordynamic problems, that is, the prediction of rotor response while passing through lower critical speeds, the extent of unstable regions and the associated stresses developed.

The advances in rotordynamic theory, computer simulations and experimental equipment are all essential in the accurate prediction of rotordynamic phenomena. As analytical methods for accurate prediction of rotordynamic response become increasing complex, it becomes apparent that an experimental platform becomes an important component for validation of analytical models and direct computer simulation. An experimental facility that effectively duplicates rotordynamic phenomena, found in modern rotating machinery, is extremely useful for laboratory investigation and educational demonstration.

Therefore, the main objective of this research was to develop an experimental facility that effectively duplicates the rotordynamic phenomena associated with rotating machinery. The rotordynamic platform consisted of a Nevada Bentley Rotor Kit with a computerized data acquisition and analysis process. The use of a self-designed LabVIEW Virtual Instrument allows for a flexible data acquisition process.

Following completion of the experimental facility, it was desired to utilize the facility in determining rotordynamic characteristics of the rotor assembly during subcritical, resonant and supercritical conditions. Experiments conducted included construction of cascade plots for a simply supported, single disk configuration with the rotor disk positioned at $1/8$, $1/4$ and $1/2$ axial positions.

Analytical modeling and prediction of the rotor assembly's first lateral natural frequency was conducted while moving the position of the rotor disk along the length of the shaft. Rayleigh's energy method and Dunkerley's formula were utilized for the upper

and lower theoretical bounds for the frequency respectively. Experimentally measured natural frequencies were then compared to this bounded region.

A Mechanical Engineering vibrations laboratory was designed to investigate the phenomena of synchronous whirl due to a mass imbalance. A demonstration of this experiment showed the rotor assembly experiencing the unique phenomena of backward whirl, as well as, oil whip

Finally, a summary of the supporting conclusions and recommendations are given. This facility can effectively duplicate rotordynamic phenomena and should be utilized for further investigation of these phenomena.

II. EXPERIMENTAL FACILITY GENERAL DESCRIPTION

The experimental facility consisted of a versatile computerized data acquisition process which precisely measured the rotor position and rotor displacement of a Bently Nevada Corporation Rotor Kit. The rotor kit is a model of high speed rotating machines that effectively duplicates the associated rotordynamic phenomena. Data acquisition was performed utilizing an IBM compatible personal computer with an internal data acquisition board and an external general purpose termination breadboard. The data acquisition process was controlled by a software driven Virtual Instrument (VI) developed using the software National Instruments LabVIEW. Proper integration of these highly technical components enhanced the development of this experimental facility which serves as a test bed for rotordynamic phenomena of rotating machinery. See Figures 1 and 2 for photographs of the facility and Figure 3 for a block diagram of the facility.

A. EXPERIMENTAL FACILITY HARDWARE

1. Bently Nevada Long Base Rotor Kit (Model 24755)

The Bentley Nevada Long Base Rotor Kit may be assembled to represent various operating configurations and conditions. The basic kit includes a rotor and base assembly with motor and rotor disk; external power supply and speed control, and sensing probes (eddy current proximeters) used to measure rotor shaft displacement. A brief description of the major components used for a simply supported, single disk rotor assembly follows. This configuration was used for all experiments conducted within.

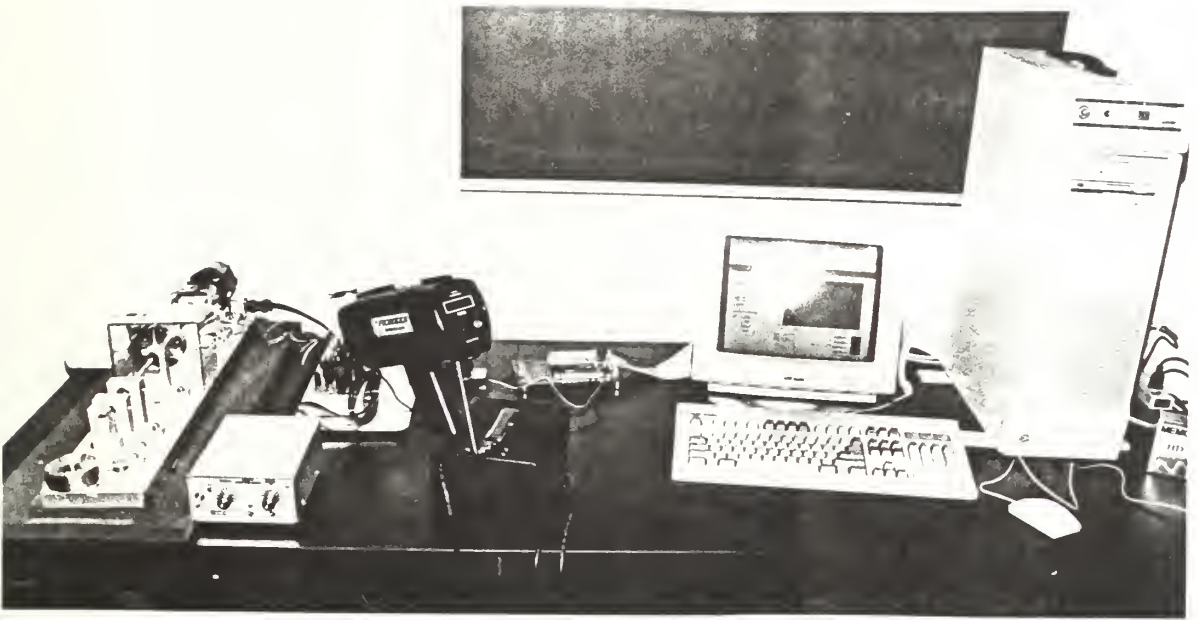


Figure 1. Photograph of the Experimental Facility.

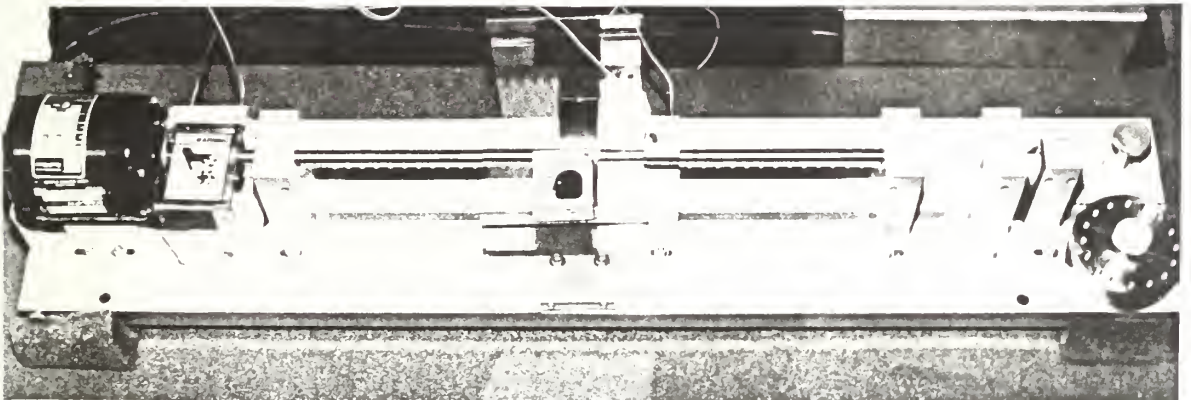


Figure 2. Photograph of the Bently Nevada Rotor Assembly in a Simply Supported, Single Disk Configuration.

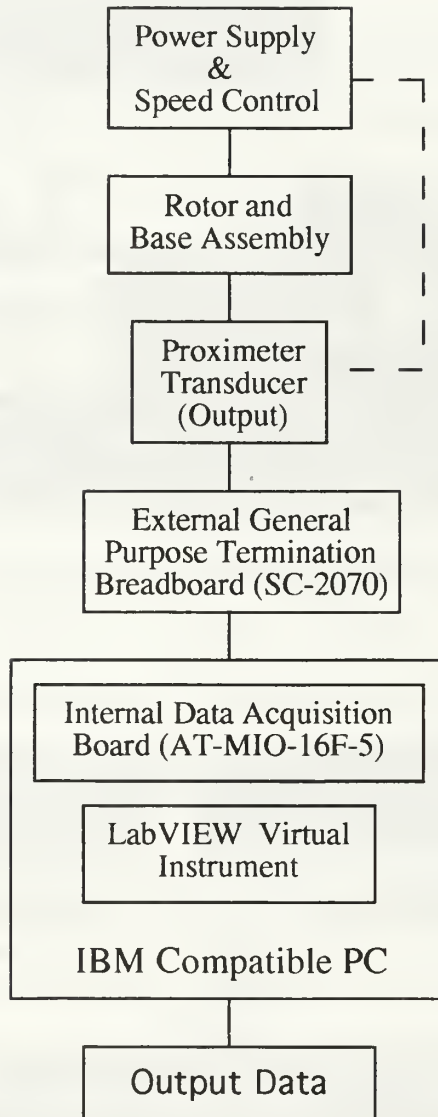


Figure 3. Block Diagram of the Experimental Facility.

a. Motor Speed Control & Power Supply

The motor speed control and power supply provides power for both the drive motor and the eddy current proximeters. The drive motor's speed can be varied from approximately 200 RPM (slow roll) up to a maximum of 11,600 RPM. The rate and direction of speed ramping, either for increasing or decreasing speed, can also be selected.

b. Rotor and Base Assembly

The Rotor and Base Assembly (Figure 4) consist of a rigid mounting base, both an inboard and an outboard bearing support, drive motor, X-Y probe mount, rotor shaft and rotor disk. The bearings are Oilite bushings (oil impregnated, sintered bronze). The rotor disk, bearing supports and probe mounts can be positioned anywhere along the rotor shaft using predrilled holes in the mounting base.

The rotor shaft is connected inline to the drive shaft motor with a flexible coupling. A single notched disk and a twelve notched disk, which provides feedback to the motor speed controller, are mounted on the drive motor shaft. These disks allow for rotor position monitoring during operation.

Specific dimensions and material properties of the components of the Rotor and Base Assembly are found in Appendix A.

c. Eddy Current Proximeters

Rotor shaft displacements are measured by eddy current proximeters. The rotor kit has the capability to power four proximeters (not including the 12 notched feedback proximeter). Proximeter output, in volts, is a function of separation between the proximeter and the rotor shaft. A proximeter calibration curve can be found in Appendix B. The proximeters are found to be linear between the range of 2 and 55 mils with a output rating of 240 mV/mil.

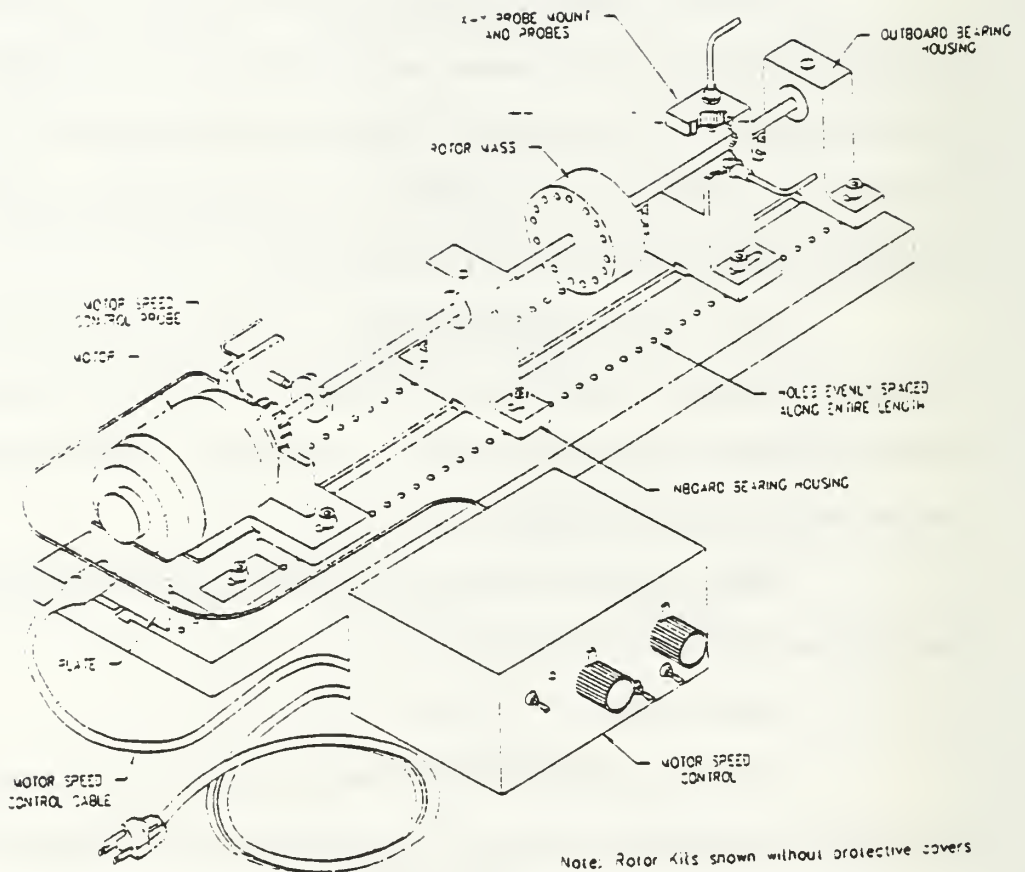


Figure 4. Bently Nevada Rotor Assembly Diagram.
 (Reprinted with permission from the Bently Nevada Corporation)

The configuration and signal connections for the proximeters are explained in Appendix C. This configuration was used for all experiments conducted.

Though not part of the rotor kit, an electrical device was designed to convert selected proximeter output to a TTL signal. The converter can handle two signals. TTL signals can be used as triggering and clocking signals for the data acquisition process, as discussed later.

2. Data Acquisition Hardware

a. NI General-Purpose Termination Breadboard (SC-2070)

The outputs of the proximeter transducers are connected to a National Instrument general-purpose termination breadboard (SC-2070). This is a device allows for the connection of analog and digital signals, as well as, triggering and scan rate signals to the data acquisition board. The SC-2070 is connected to the data acquisition board via a 50-Pin Input/Output Connector. Silk-screened component locations for resistors and capacitors are available to build filters and voltage dividers. The board also has a general purpose breadboard area for custom circuit design. [Ref. 1]

The board has the capability to connect eight differential or 16 single-ended analog input channels to the data acquisition board. For all experiments, differential configuration was utilized, thus limiting input eight to channels. Channel designation is found in Table I.

When required, external trigger signals are connected to the board's EXT TRIG* terminal and external scan rate or clocking signals are connected to the board's OUT2 terminal. The grounding connection for both of these external signals is the digital ground or DGND terminal.

**TABLE I. SC-2070 DIFFERENTIAL INPUT
CHANNEL DESIGNATIONS**

Channel Designations	
Differential Channel	Input Terminals
0	0,8
1	1,9
2	2,10
3	3,11
4	4,12
5	5,13
6	6,14
7	7,15

b. NI Data Acquisition Interface Board (AT-MIO-16F-5)

The NI Data Acquisition Interface Board (AT-MIO-16F-5) is an internal high-performance multifunction analog, digital and timing I/O board for the personal computer. It uses 12-bit sampling ADC with the capability to sample data at a 200 ksamples/sec over the 16 single-ended or eight differential analog input channels described earlier. It has the capability for either digital or software triggering. The board is installed in a 16-bit expansion slot in the computer. It has an onboard DAC reference voltage of 10 V, called AGND, any signal greater than +12 V with respect to this reference voltage will saturate internal components and result in distorted data. Configuration and control of the data acquisition board is performed utilizing NI LabVIEW for Windows software. See Appendix D for actual configuration procedures and default parameters. [Ref. 2]

c. DataStor IBM Personal Computer and HP Inkjet Printer

The DataStor IBM personal computer is a 486DX2 computer with CPU speeds of 66 MHz or 20 MHz, 16M RAM and a 515M hard drive. Connected to the parallel port LPT1 is a HP Inkjet 550C printer.

d. Optical Stroboscope

The use of an optical stroboscope allowed for the accurate determination of rotor speed since the motor speed controller does not have precise speed indications. Reflective tape was placed on the face of the rotor disk.

B. EXPERIMENTAL FACILITY SOFTWARE

1. Computer Operating Systems

The disk operating system installed on the computer is MS-DOS 6.0. Additionally, Windows 3.1 is installed and required for the data acquisition software.

2. Data Acquisition Software

The software used to control the data acquisition process was National Instruments LabVIEW for Windows version 3.0. LabVIEW is a program development application which uses a graphical programming language, called G, to create programs in block diagram form. It is designed specifically for data acquisition and instrument control.

LabVIEW programs are called virtual instruments (VI's) because their appearance and operation imitate actual instruments. There are two main parts of a VI, the front panel and the block diagram.

The front panel is the user interface portion of a VI. It acts like the panel of an actual instrument. It contains controls and indicators. Controls simulate instrument input devices. They supply data to the block diagram. Indicators simulate instrument output devices. They display data acquired or generated by the block diagram.

The block diagram is the graphical source code or program of a VI. It is constructed by 'wiring' together operators, functions or even SubVI's, which ultimately control the flow of program execution.

The virtual instrument designed for the control of the data acquisition processes for the experiments to follow is called ROTOR.VI. This VI is a hardware timed, software

triggered, circular buffered I/O process. This VI was utilized for the acquisition, display and storage of proximeter output. Required inputs, operating procedures and VI outputs are described in Appendix E.

III. ROTOR CHARACTERISTICS: CASCADE PLOTS

Cascade plots are effective tools that can be use to determine the general fundamental rotor characteristics and the rotordynamic phenomena experienced during subcritical, resonant and supercritical operation of the rotor assembly. Cascade plots were constructed for the rotor assembly for several positions of the rotor disk. A cascade or waterfall plot is constructing by 'stacking' the power spectral densities of the time trace signal corresponding to rotor speeds over the desired range of operation. Information such as the first lateral natural frequencies, excitation of rotor sub-harmonics and super-harmonics, oil whirl and oil whip conditions, as well as, many other phenomena can be observed from the plots.

A. ROTOR ASSEMBLY CONFIGURATION

The rotor kit was configured as a simply supported, single disk configuration, with a mass imbalance attached. The inboard and outboard bearing supports were set 17 inches apart, leaving one half inch overhang on each end. The rotor disk had a two gram mass imbalance attached. Experiments were conduct with the rotor disk was positioned at 8.5, 4.25 and 2.125 inches from the inboard bearing support.

The virtual instrument used to control the data acquisition process was ROTOR.VI. For an explanation of ROTOR.VI, see Appendix E. The number of scans was 1024 with a sampling frequency of 2048 samples/sec. The x and y-displacements versus time data were collected for rotor speed ranging from 300 RPM to 10,000 RPM, incrementing every 200 RPM. Figure 5 is an example of the y-displacement time traces for a rotor speed of 5560 RPM.

The time domain signals of the y-displacements voltages were formatted into a matrix with rows corresponding to each rotor speed (run number) and columns corresponding to the scan number. The DC component of the signal was subtracted, resulting in zero mean data, and then converted from voltage to mils using a calibration factor. Each time domain data point was then converted into the frequency domain by taking the Discrete Fourier Transform (FFT). Since dealing with FFT's, it is required that the number of scans be a multiple of two. The power spectral density (PSD) was then calculated using

$$PSD = \frac{\sqrt{FFT * conj(FFT)}}{2N} \quad (1)$$

where N = number of scans (1024).

The resulting units of the PSD matrix are mils per Hz. Figure 6 is an example of the PSD curve of the y-displacement voltage for a rotor speed of 5560 RPM. Plotting the matrix in 3-D by using a MATLAB Waterfall command, plots the PSD curve for each rotor speed successively. This results in PSD magnitude along the vertical y-axis, frequency along the x-axis and rotor speed along the z-axis. Using a view command of view(0,45), rotates the plot such that a 2-D cascade plot is obtained with the frequency along the horizontal axis, PSD magnitude along the left vertical axis and rotor speed along the right vertical axis.

Cascade plots were generated for each rotor mass location, over the operating speed range.

B. DISCUSSION OF THE RESULTS

1. Rotor Disk at a=8.5 inches: Centered

Cascade plots with the rotor disk position at the center of the rotor shaft are shown in Figure 7. These plots clearly show a synchronous whirl condition along the first order

response. For this configuration, peak response indicates the first lateral natural frequency (ω_n) to be 2250 RPM. Additionally, the second order (2x) super-harmonic can be seen for a majority of the running speeds. For rotor speeds near ω_n , the second, third (3x) and fourth (4x) order super harmonics are also excited. Also, as the rotor speed approached twice ω_n , nonlinearities develop causing the one half order ($1/2 x$) sub-harmonic to be excited. This could be the beginning of an oil whirl condition.

2. Rotor Disk at a=4.25 inches: 1/4 Axial

The rotor disk's distance from the inboard bearing was decreased in half. The cascade plots with the rotor disk positioned at a=4.25 inches are shown in Figure 8. These plots show all phenomena as in for the plots for a=8.5 inches described above. For this configuration, peak response indicates ω_n to be 2700 RPM. The oil whirl condition along the ($1/2 X$) subharmonic continues though indications are not as prevalent.

3. Rotor Disk at a=2.125 inches: 1/8 Axial

The distance from the outboard bearing was once again decreased in half. The cascade plots with the rotor disk positioned for a =2.125 inches are shown in Figure 9. These plots show all phenomena as in for the plots for a=8.5 and a=4.5 inches described above. For this configuration, peak response indicates ω_n to be 3700 RPM. Additionally, an second critical speed was observed along the synchronous speed line at 8400 RPM. The amplitude between critical speeds remain relatively high. For speeds greater than the second critical speed, the amplitude decreases significantly. Once again, as the rotor speed approaches twice ω_n , the one half order ($1/2 x$) subharmonic is excited. At speeds slightly greater than ω_n , this unstable condition continues along a frequency equal to ω_n vice along the one half order subharmonic. This follows the characteristics of an oil whip condition.

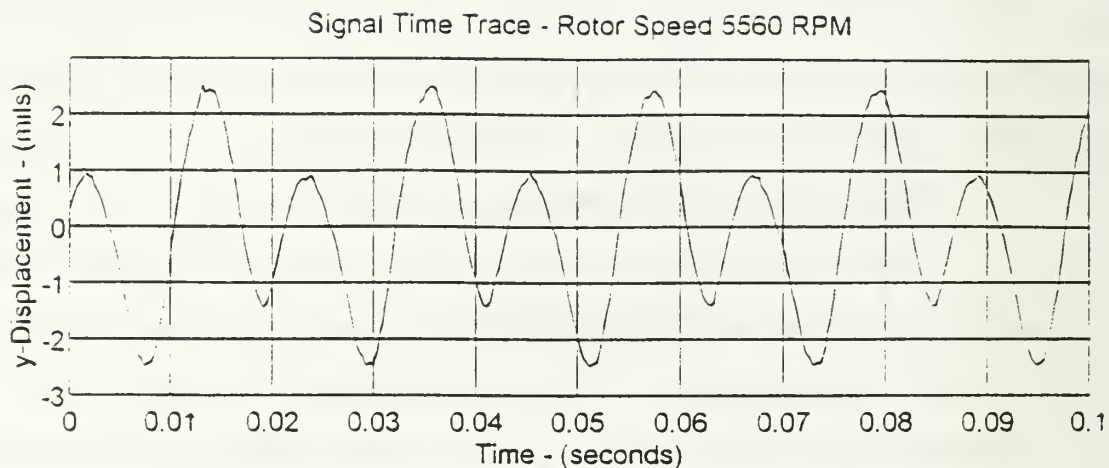


Figure 5. Time Trace for the Y-Displacement for a Rotor Speed of 5560 RPM. Rotor Assembly in a Simply Supported, Single Disk Configuration, Rotor Length of 17.0 Inches, Disk Located 8.5 Inches from the Inboard Bearing Support with a 2 Gram Mass Imbalance.

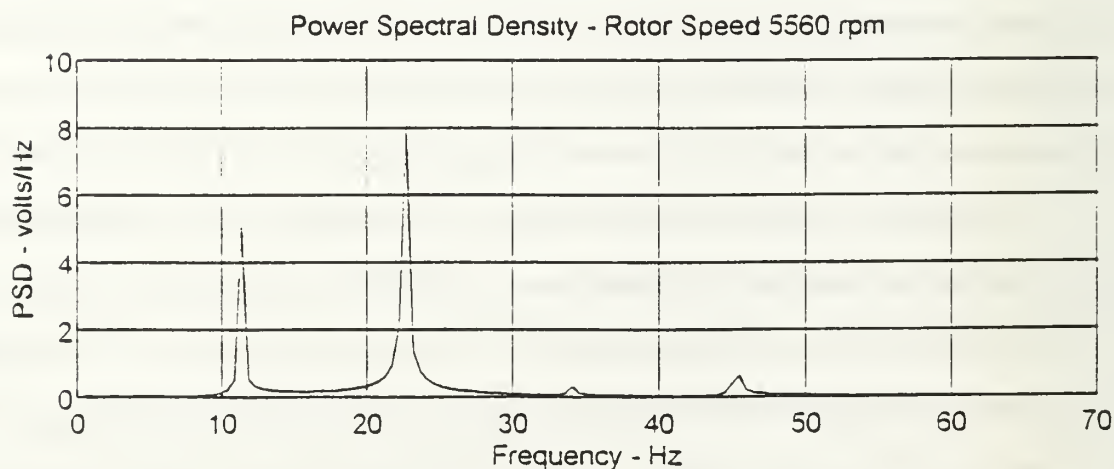


Figure 6. The Power Spectral Density Plot of the Y-Displacement Time Trace Shown Above in Figure (5).

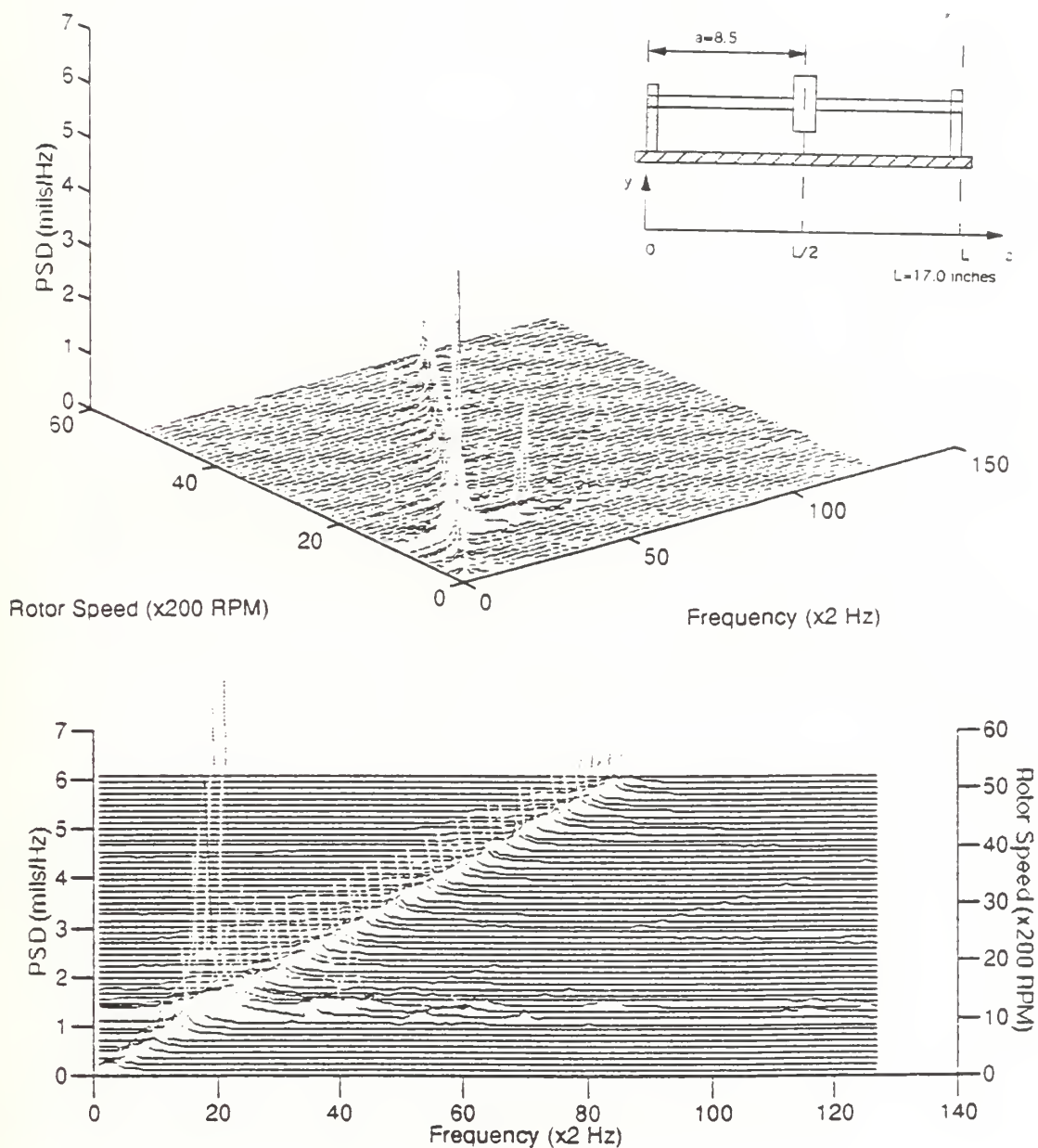


Figure 7. Cascade Plots of the Rotor Assembly in a Simply Supported, Single Disk Configuration, Rotor Length of 17.0 Inches, Disk Located 8.5 Inches from the Inboard Bearing Support with a 2 Gram Mass Imbalance.

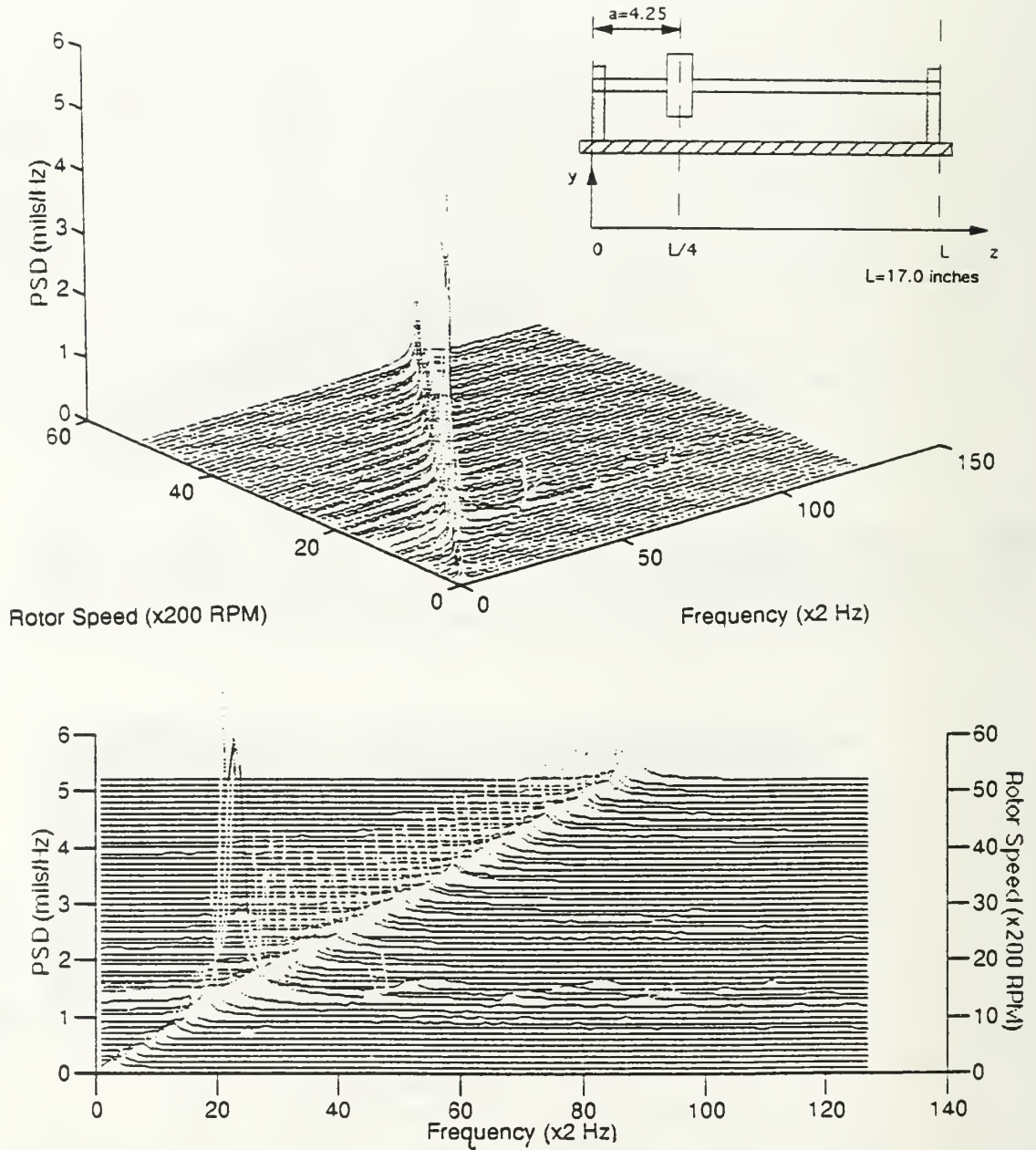


Figure 8. Cascade Plots of the Rotor Assembly in a Simply Supported, Single Disk Configuration, Rotor Length of 17.0 Inches, Disk Located 4.25 Inches from the Inboard Bearing Support with a 2 Gram Mass Imbalance.

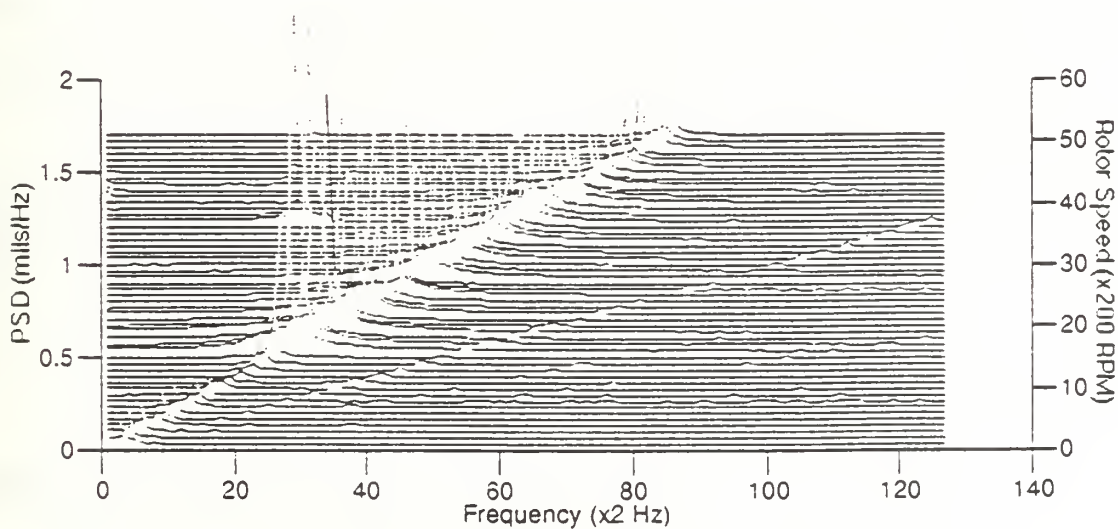
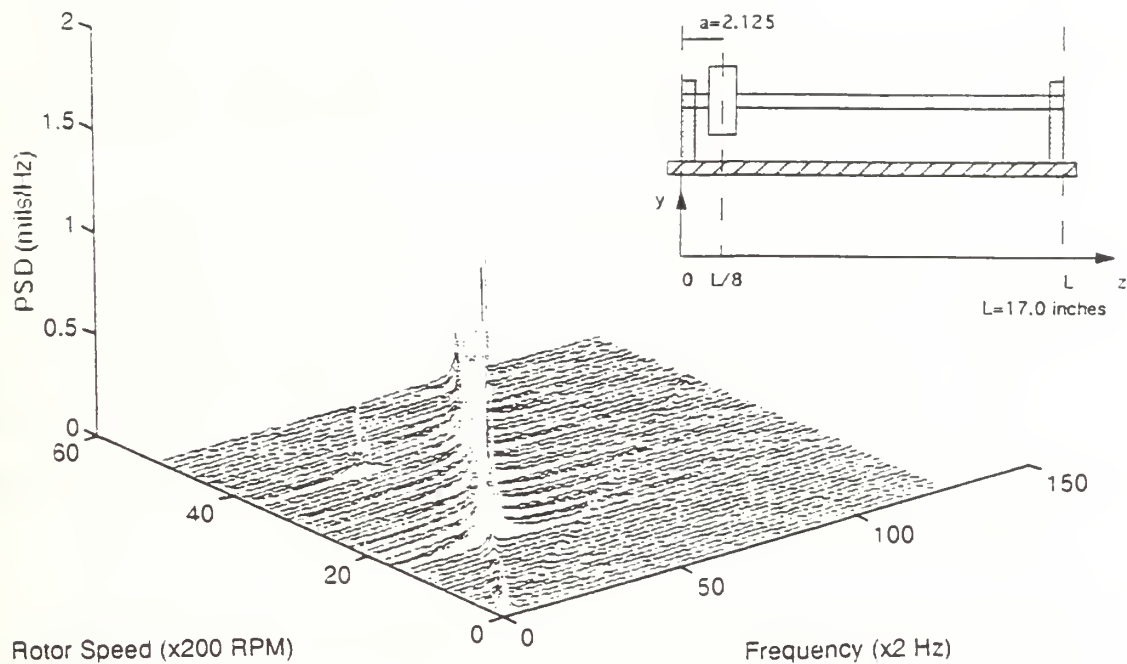


Figure 9. Cascade Plots of the Rotor Assembly in a Simply Supported, Single Disk Configuration, Rotor Length of 17.0 Inches, Disk Located 2.125 Inches from the Inboard Bearing Support with a 2 Gram Mass Imbalance.

IV. ANALYTICAL PREDICTION OF THE FIRST LATERAL MODE

The position of the rotor disk and its effect on the first lateral natural frequency was of interest. Theoretical predictions for the bounded region of ω_n was first completed using Rayleigh's energy method for the upper bound and Dunkerley's formula for the lower bound. An experimental measured ω_n was determined for the rotor assembly as the position of the rotor disk moved along the rotor shaft. Comparison of the experimental ω_n and the theoretical bounded range was then conducted.

A. ROTOR ASSEMBLY CONFIGURATION

The rotor kit was configured as a simply supported, single disk configuration, with a mass imbalance attached. The inboard and outboard bearing supports were set 14.5 inches apart, with the outboard bearing support flushed with the rotor shaft's end. The rotor disk had a two gram mass imbalance attached.

The rotor disk was positioned at positions symmetric to the center of the rotor shaft ($a=2.0, 3.0, 4.0, 5.0, 6.0, 7.0, 7.5, 8.5, 9.5, 10.5, 11.5, 12.5$ inches). The virtual instrument used to control the data acquisition process was ROTOR.VI. The default parameters for the VI inputs were utilized.

B. THEORETICAL UPPER BOUND: RAYLEIGH'S ENERGY METHOD

Rayleigh's energy method for determining the first lateral natural frequency of a system provides a theoretical upper bound for the frequency. Rayleigh's energy method neglects damping and assumes that the total energy of a system is conserved.

$$T_{\max} = U_{\max} \quad (1)$$

The rotor assembly was modeled as a simply supported beam (pinned-pinned) with the rotor mass treated as an applied load, as seen in Figure 10.

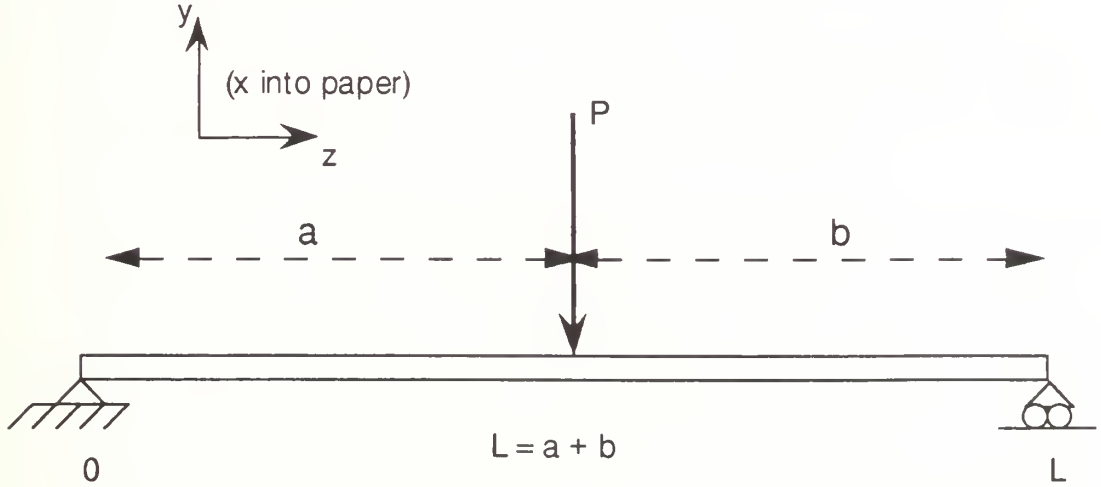


Figure 10. Rotor Assembly Model.

As derived in [Ref. 3], the maximum kinetic energy and maximum potential energy of the shaft and disk are

$$T_{\max} = \frac{\gamma}{2} \int_0^L (y(z)\omega_n)^2 dz + \frac{m}{2} (y(z=a)\omega_n)^2 \quad (2)$$

$$U_{\max} = \frac{EI}{2} \int_0^L \left(\frac{d^2 y(z)}{dz^2} \right)^2 dz \quad (3)$$

where E = the modulus of elasticity of the rotor shaft

I = the first moment of inertia of the rotor shaft

L = length of the rotor shaft

γ = weight density of the rotor shaft

m = mass of the rotor disk mass

$y(z)$ = shape function

Substituting equations (2) and (3) into equation (1) and solving for the first lateral natural frequency yields

$$\omega_n = \left[\frac{EI \int_0^L \left(\frac{d^2 y(z)}{dz^2} \right)^2 dz}{\gamma \int_0^L (y(z) \omega_n)^2 dz + m(y(z=a) \omega_n)^2} \right]^{\frac{1}{2}} \quad (4)$$

The shape function used was the static deflection equations for a simply supported beam with a concentrated load

$$y(z) = \frac{Pbz}{6EIL} (L^2 - z^2 - b^2) \quad \text{for } z \leq a \quad (5)$$

$$y(z) = \frac{Pb}{6EIL} \left[(L^2 - b^2)z - z^3 + \frac{L}{b}(z-a)^3 \right] \quad \text{for } z \geq a \quad (6)$$

The first lateral natural frequency was determined while varying the location of the rotor disk utilizing a computer program for MathCAD 3.0 for Windows. MathCAD's has the ability to evaluate derivatives and integrals directly.

C. THEORETICAL LOWER BOUND: DUNKERLEY'S FORMULA

Dunkerley's formula for determining the first lateral natural frequency provides a theoretical lower bound for the frequency.

As in the Rayleigh's Energy method, the rotor assembly can be modeled as a simply supported beam (pinned-pinned) with the rotor mass treated as an applied load, see Figure 10.

As derived in [Ref. 4], Dunkerley's formula for the rotor assembly can be written as

$$\frac{1}{\omega_n^2} = \frac{1}{\omega_{11}^2} + \frac{1}{\omega_{22}^2} = \frac{1}{\omega_{11}^2} + a_{22}m \quad (7)$$

where ω_n = the fundamental frequency of the rotor shaft and rotor mass

ω_{11} = the fundamental frequency of the rotor shaft by itself

ω_{22} = the natural frequency of the rotor mass mounted on the rotor shaft in the absence of other masses

a_{22} = the influence coefficient due to a unit load applied at the location of the rotor disk

m = the mass of the rotor disk.

Solving equation (7) for the first lateral natural frequency yields

$$\omega_n^2 = \frac{\omega_{11}^2}{1 + a_{22}m\omega_{11}^2} \quad (8)$$

For a simply supported beam of uniform mass, M , the fundamental frequency of the rotor shaft is

$$\omega_{11}^2 = \pi^4 \left(\frac{EI}{ML^3} \right) \quad (9)$$

The influence coefficient can be determined from the static deflection equation for a simply supported beam evaluated at $z = a$.

$$a_{22} = y(z = a) = \frac{Pba}{6EIL} (L^2 - a^2 - b^2) \quad (10)$$

The first lateral natural frequency was determined while varying the location of the rotor disk utilizing a computer program for MATLAB.

D. DISCUSSION OF RESULTS

The theoretical bounded range of ω_n versus disk position are plotted along with the experimental values, see Figure 11. As seen from the plot, the experimentally measured ω_n fell between the bounded region for values of rotor disk position between five and nine inches. As the rotor disk position was moved towards either bearing support, the experimental ω_n began to fall below the bounded range. The percent deviation from theoretical values increased as the rotor disk was moved closer to the bearing supports.

The reason for deviation from theoretical values can be attributed to the flexibility (stiffness) of the bearing supports and their effect of the rotor assembly. When the rotor disk is placed near the center of the shaft, the stiffness and damping of the bearing supports apparently have very little, if any, effect on the ω_n of the rotor assembly and may be modeled as pinned connections. As the rotor disk is placed closer to a bearing support, the effects of the bearing supports' flexibilities play a larger role in the vibration characteristics of the rotor assembly. Therefore, the bearings can no longer be modeled as pinned connections but as springs (added flexibility), which would now account for the energies of the bearing supports.

Additionally, with these extra stiffness terms, the first mode shape of vibration will differ from the typical first bending mode associated with the pinned-pinned model. The mode shape is most likely a combination of bending, bouncing and rocking modes, with the bouncing and rocking mode having more of an effect as the disk is moved closer to the support. Therefore, using the static deflection as a mode shape is not representative of the actual mode shape when the disk is placed near the bearing supports, thus, increasing the theoretical error. Though, the shape function selected need not have the exact shape of the mode shape to obtain a good approximation, the accuracy of the theoretical values increases as the shape function used most resembles the actual mode shape [Ref. 4].

The theoretical bounded range was symmetric about the rotor shaft center, the experimental values were asymmetric. It can be concluded that the vibrational properties of the two bearings supports are different. Different stiffness values for the two bearing supports add to the complexity of the mode shape.

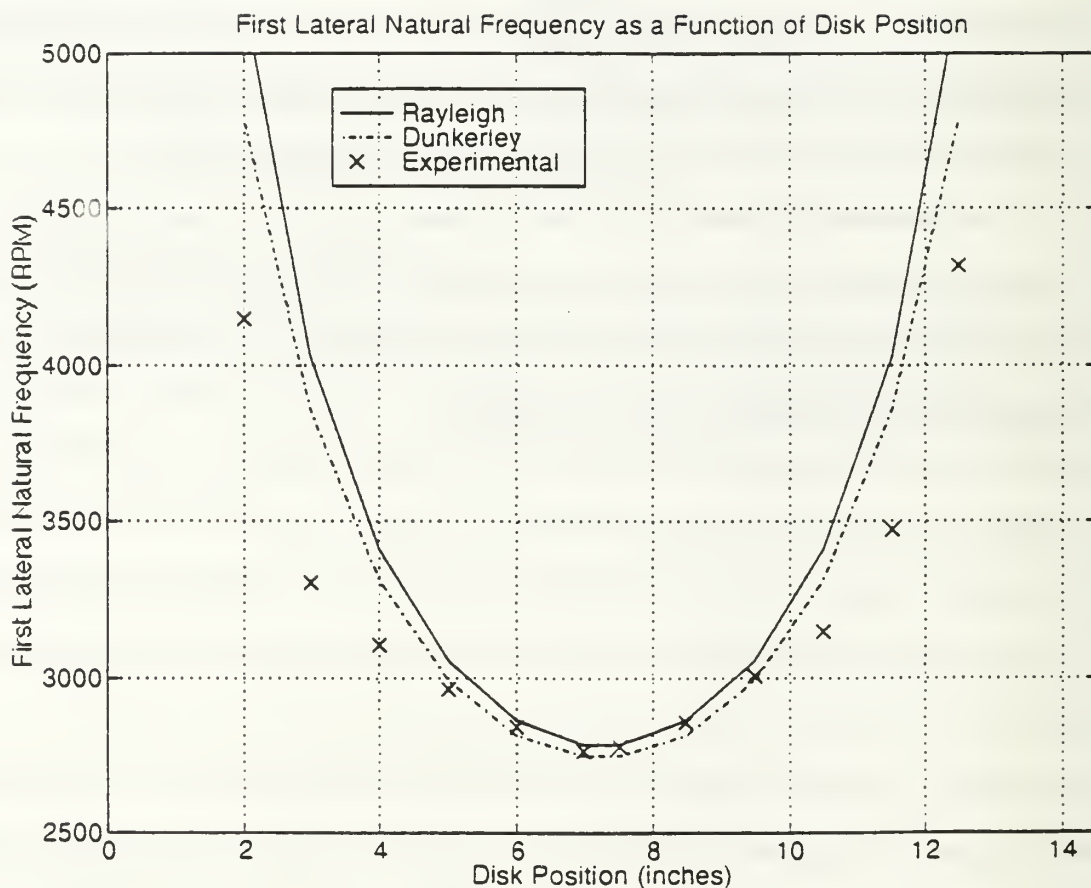


Figure 11. Theoretical and Experimental First Lateral Natural Frequency as a Function of Rotor Disk Position. The Rotor Assembly is in a Simply Supported, Single Disk Configuration, Rotor Length of 14.5 Inches, Disk with a Two Gram Mass Imbalance.

V. SYNCHRONOUS WHIRL DUE TO A MASS IMBALANCE

It was desired to develop a Mechanical Engineering vibration laboratory for the phenomena of synchronous whirl due to a mass imbalance. The objective was to experimentally measure and observe the phenomena of synchronous whirl due to a mass imbalance during subcritical, resonant and supercritical operation of the rotor assembly.

A. THEORETICAL BACKGROUND: SYNCHRONOUS WHIRL

The behavior of rotor-bearing systems was first analyzed by Rankine in 1869. He incorrectly predicted that the operating speeds could never exceed the first critical speed [Ref. 5]. The phenomena of synchronous whirl excited by a mass imbalance was later addressed by Jeffcott [Ref. 6]. Jeffcott explained that while an unbalanced shaft rotates about its longitudinal axis, the shaft will bend and, thus, whirl about the bearing axis (AB), see Figure 12. As the name implies, the whirl speed is equal to the rotational speed of the rotor.

The amount of bending or whirl radius is dependent upon the center of mass offset (q), rotating speed (ω) and its nearness to ω_n . The steady-state solution of the differential equations of motion for this system yields equal shaft displacements in the x and y directions, resulting in circular whirl orbits of radius (R) [Ref. 7].

$$R = \sqrt{x^2 + y^2} = \frac{q \left(\frac{\omega}{\omega_n} \right)^2}{\sqrt{\left(1 - \left(\frac{\omega}{\omega_n} \right)^2 \right)^2 + \left(2\zeta \left(\frac{\omega}{\omega_n} \right) \right)^2}} \quad (12)$$

Synchronous Whirl Condition.

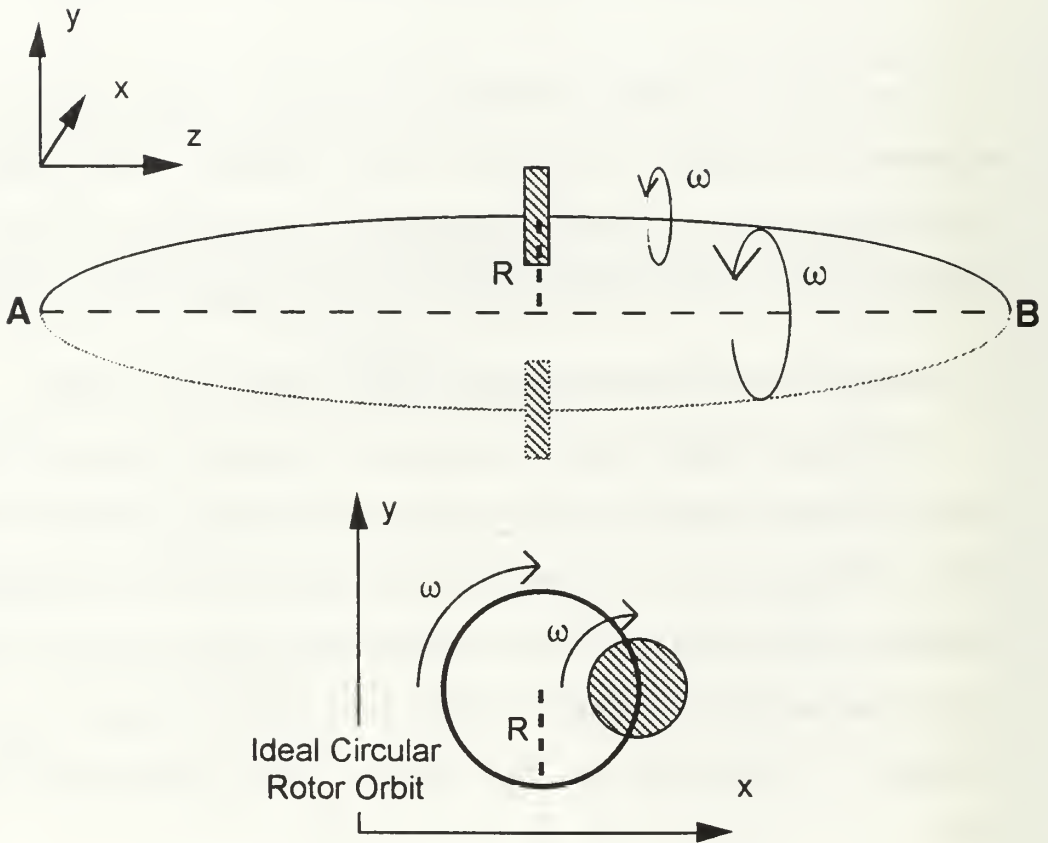


Figure 12. Synchronous Whirl and Synchronous Whirl Orbit.

Another characteristic associated with synchronous whirl is a phase shift between the mass imbalance (a fixed rotor position) and the maximum shaft displacement. As the shaft whirls, the maximum displacement will begin to lag the mass imbalance. The amount of phase lag (λ) also depends on the rotating shaft speed and its nearness to the first lateral natural frequency. [Ref. 7]

$$\lambda = \tan^{-1} \left(\frac{-2\zeta \left(\frac{\omega}{\omega_n} \right)}{1 - \left(\frac{\omega}{\omega_n} \right)^2} \right) \quad (13)$$

Typical plots of whirl radius or shaft displacement and phase lag versus rotating shaft speed are shown in Figure 13 for a system with slight damping.

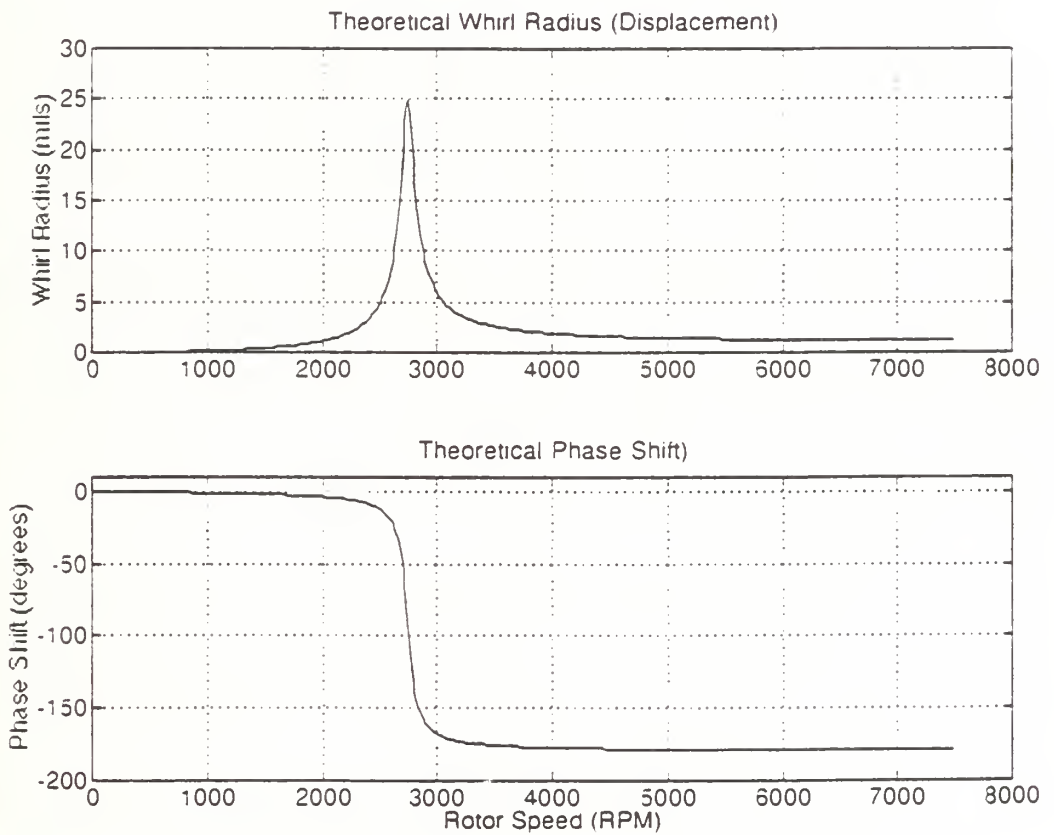


Figure 13. Theoretical Plots of the Whirl Radius (R) and the Maximum Displacement-Mass Imbalance Phase Lag (λ) Versus Rotor Speed for a System with Slight Damping.

B. EXPERIMENTAL CONFIGURATION

1. Rotor Assembly

The rotor assembly was in a simply supported, single disk configuration. The bearing supports were positioned 14.5 inches apart ($L=14.5$) with the outboard bearing support flushed with the rotor shaft end. The rotor disk was centered between the bearing supports, 7.25 inches from either bearing support, with the zero degrees position hole aligned with the single notched disk. A mass imbalance of 1.6 grams was placed at the zero degrees position. With the mass imbalance aligned with the single notched disk, rotor position corresponds to the mass imbalance position. For initial balancing of the rotor assembly, a 0.25 gram mass was positioned at the 315 degrees position.

2. Proximeter Connections

An X-Y probe mount was placed 1.5 inches from the inboard bearing support. This probe mount position ensures that the vibrating rotor shaft does not contact the proximeter during operation. The connections for the proximeters are listed in Appendix C.

3. Stroboscope

A stroboscope is required for precise measurement of rotor speed throughout the experiment. Reflective tape was placed on the face of the rotor disk mass.

4. Virtual Instrument

With the NI AT-MIO-16f-5 Multifunction I/O board configured for differential input as discussed in Appendix D, the virtual instrument, ROTOR.VI, was utilized with the default input parameters. See Appendix E for a description of ROTOR.VI.

C. DISCUSSION OF THE RESULTS

The VI was ran for speeds ranging from 380 RPM up to 7000 RPM. Increments of speed varied from 300 RPM to 20 RPM, utilizing the smaller increments for speeds near the higher amplitude signals. The rotor is driven by the drive motor in a clockwise direction, considered the positive direction.

For each run, the rotor speed and the phase shift between the maximum y-displacement and mass imbalance were recorded, as well as, sending the raw data to the computer hard drive. Appendix F contains a list of rotor speeds and corresponding data files for which the experiment was conducted.

1. Maximum Rotor Displacement Versus Rotor Speed

The maximum y-displacements versus rotor speed were plotted in Figure 14. Compared to the theoretical expectations of Figure 13, the results resemble a typical plot for a system with slight damping. The first lateral natural frequency determined from peak displacement for this experiment was 2740 RPM.

Observation of the rotor orbit on the front panel of the VI showed that the orbit was not circular but elliptic during operation near ω_n . Therefore, the x-displacements and the y-displacements were not equal as originally expected. Utilizing the raw data, maximum x-displacement versus rotor speed was also plotted. This x-displacement indicated a critical peak at 2900 RPM. A plot of the major radius of the elliptical orbit (R) versus the rotor speed showed these two critical peaks or a double critical condition. See Figure 15.

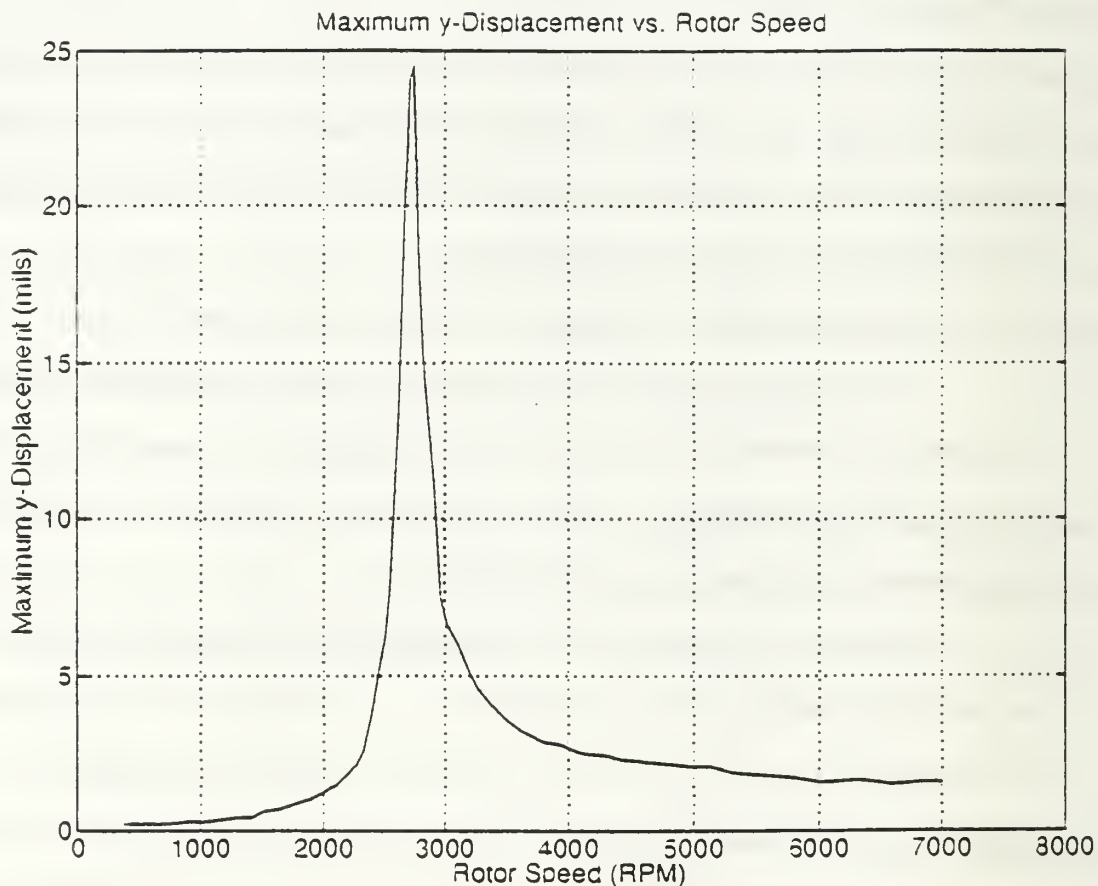


Figure 14. Experimental Results of the Maximum Y-Displacement Versus Rotor Speed. The Rotor Assembly is in a Simply Supported, Single Disk Configuration, Rotor Length of 14.5 Inches, Disk Located 7.25 Inches from the Inboard Bearing Support (Centered) with a 1.6 Gram Mass Imbalance.

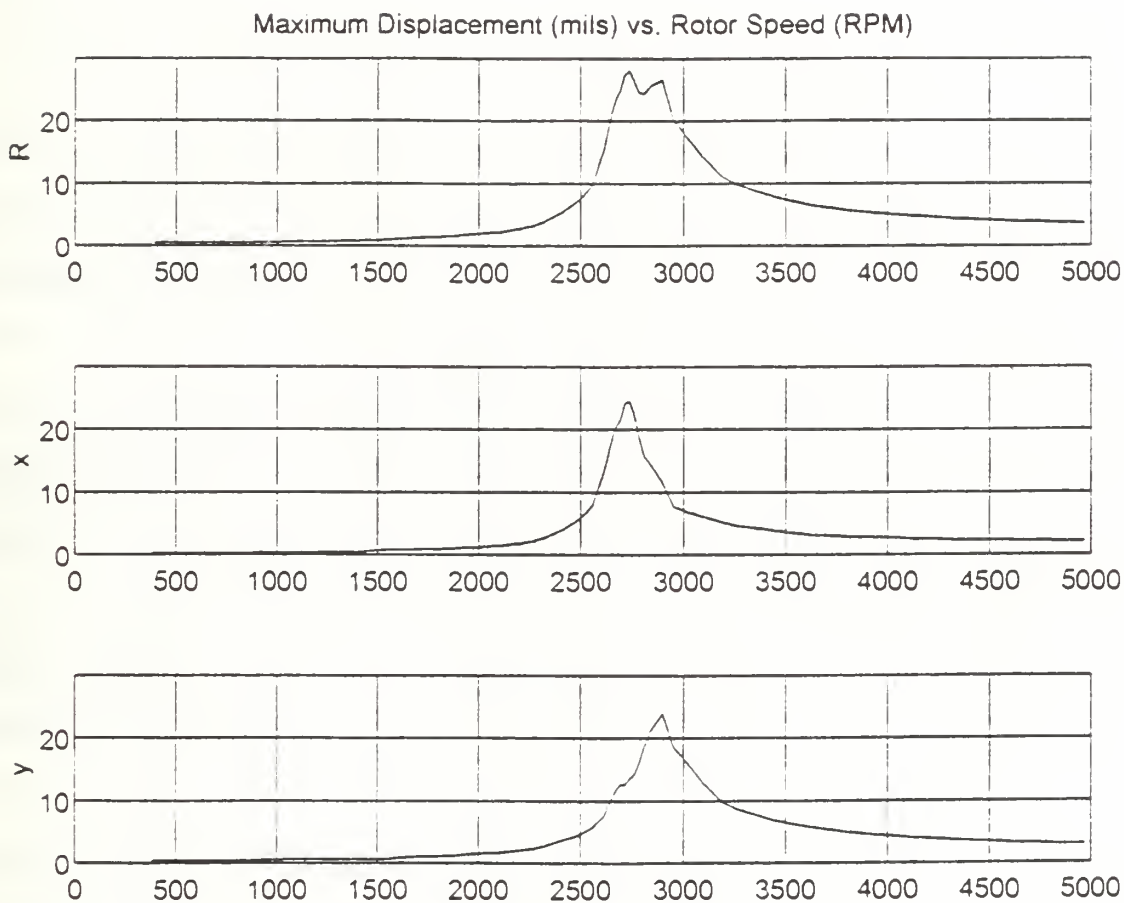


Figure 15. Experimental Results of the Whirl Orbit Major Radius (R), Maximum Y-Displacement and Maximum X-Displacement Versus Rotor Speed. The Rotor Assembly is in a Simply Supported, Single Disk Configuration, Rotor Length of 14.5 Inches, Disk Located 7.25 Inches from the Inboard Bearing Support (Centered) with a 1.6 Gram Mass Imbalance.

2. Rotor Orbit Characteristics

Utilizing the raw data sent to the computer hardrive, the x-direction and the y-direction voltages where converted to zero mean displacements by subtracting away the DC voltage component and then converting to mils. This allowed for detailed observation of the rotor orbit caused by synchronous whirl during subcritical, critical and supercritical speeds. As stated earlier, the first critical speed was determined to be 2740 RPM.

a. Subcritical Speeds

For rotor speeds between 300 and 1800 RPM, the rotor orbit was nearly circular, centered about the bearing axis. The radius of orbit increased in magnitude as rotor speed was increased. The direction in which the rotor traveled around these circular orbits was clockwise, thus undergoing forward whirl.

As speed was increased from 1800 RPM, the rotor orbit changed from circular to elliptic with the major axis of the ellipse lying 60 degrees from the x-axis, see Figure 16. With increasing speeds, the orbit became more elliptical, that is, the major axis increased in magnitude and the minor axis decreased in magnitude. The angle of the major axis continued to be approximately 60 degrees from the x-axis. The rotor continued to experience forward whirl and traveled around these elliptical orbits in a clockwise direction.

b. Critical Speed

At the first critical speed (2740 RPM), determined by peak y-displacement, the orbit was elliptic, with the major axis at its maximum magnitude and at an angle of 60 degrees from the x-axis. See Figure 17. The rotor continued to experience forward whirl.

c. Supercritical Speeds

The first rotor speed measured after the first critical speed was 2760 RPM. At this speed, the rotor orbit nearly resembled an straight line with an angle slightly less than that of the critical speed orbit. With continued small increments of speed, the orbits again became elliptic with the major axis slightly decreasing in magnitude and the minor axis

increasing in magnitude. The rotor reversed its direction of travel and now traveled around the elliptic orbits in a counter-clockwise direction. Therefore experiencing *backward whirl*, which means the precession is in the opposite sense than the shaft spin. Further increases of speeds up to the second critical peak, 2900 RPM, showed the elliptic orbits once again increasing its major axis and decreasing its minor axis until the orbit, once again, approximately resembled a straight line path. It is here, at the second critical peak, that the rotor again reverses its direction of orbital travel and reverts to traveling around the orbits in a clockwise direction. Once again undergoing forward whirl. This phenomena of two whirl direction reversals occurred within approximately 160 RPM following passage through the first critical speed. The angle of the major axis continued to rotate towards the x-axis. See Figure 18.

As rotor speed was increased further, the orbits began to become less elliptic and continued to rotate their major axis towards the x-axis. This continued until the orbits became nearly circular once again at approximately 4000 RPM. See Figure 19.

The orbits remained circular with a converging radius for the remaining runs with the exception of speeds near twice ω_n . As seen from Figure 20, at 5560 RPM the rotor is experiencing synchronous and subsynchronous whirl. A power spectral density analysis of this signal indicates the synchronous frequency of 5560 RPM and the subsynchronous frequency of the first lateral natural frequency, ω_n (2740 RPM). This phenomena follows the characteristics of an oil whip condition, also seen in the cascade plots described earlier in Chapter III.

3. Maximum Y-Displacement - Mass Imbalance Phase Shift

The phase shift between the y-displacement and the mass imbalance position was plotted versus rotor speed, see Figure 21. The experimental results resemble a typical plot for a system with slight damping. For rotor speeds $\ll \omega_n$ (2740 RPM), the displacement and mass imbalance were in phase. As the rotor speed was increased towards ω_n , the

displacement curve began to lag the mass imbalance. The phase shift increased slightly at first (30 degrees in 800 RPM's) but then increased sharply as the rotor speed approached ω_n . At ω_n , the phase shift was measured to be approximately 90 degrees lagging, as expected. As speed was increased further, the phase shift continue to increase sharply to 160 degrees lagging and then slowly approached 180 degrees lagging.

D. BACKWARD WHIRL

The phenomena of backward whirl is explained by Vance using a simple two degree of freedom model with asymmetric, uncoupled bearing support stiffnesses. His model shows that the two critical speeds result from the uncoupled, asymmetric stiffnesses of the bearings. Backward whirl is experienced when the rotor speed is between the two critical peaks, as shown by the time rate of change of the whirl angle being negative or of opposite sense of the direction of shaft rotation. [Ref. 8]

A more complex analytical model along with supporting experimental results was published by Subbiah, Bhat and Sankar. They used a six degree of freedom model with coupled, asymmetric bearings. Their experimental set-up contained a rotor with two identical hydrodynamic bearings at the ends. Again, they showed that the phenomena of backward occurred between the two critical speeds. [Ref. 9]

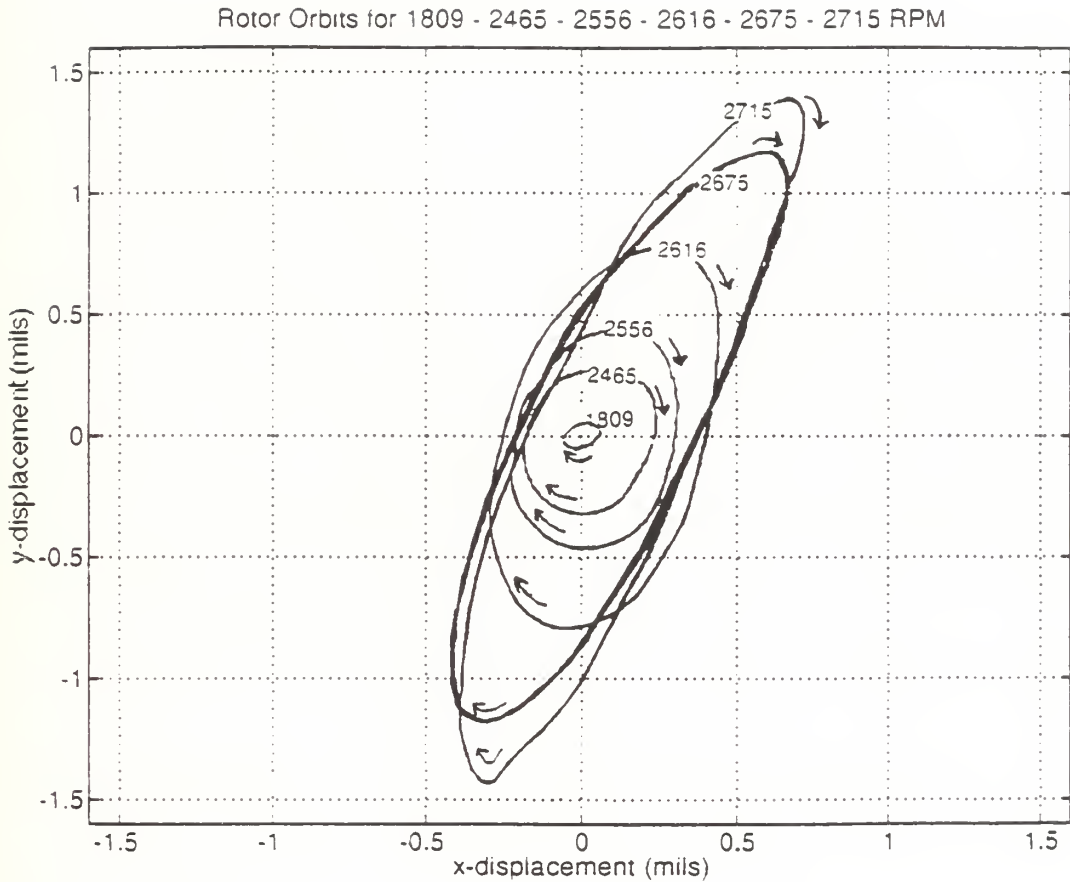


Figure 16. Rotor Orbits for Speeds Subcritical Speeds of 1809-2465 - 2556 - 2616 - 2675 - 2715 RPM. The Rotor is Experiencing Forward Whirl. The Rotor Assembly is in a Simply Supported, Single Disk Configuration, Rotor Length of 14.5 Inches, Disk Located 7.25 Inches from the Inboard Bearing Support (Centered) with a 1.6 Gram Mass Imbalance.

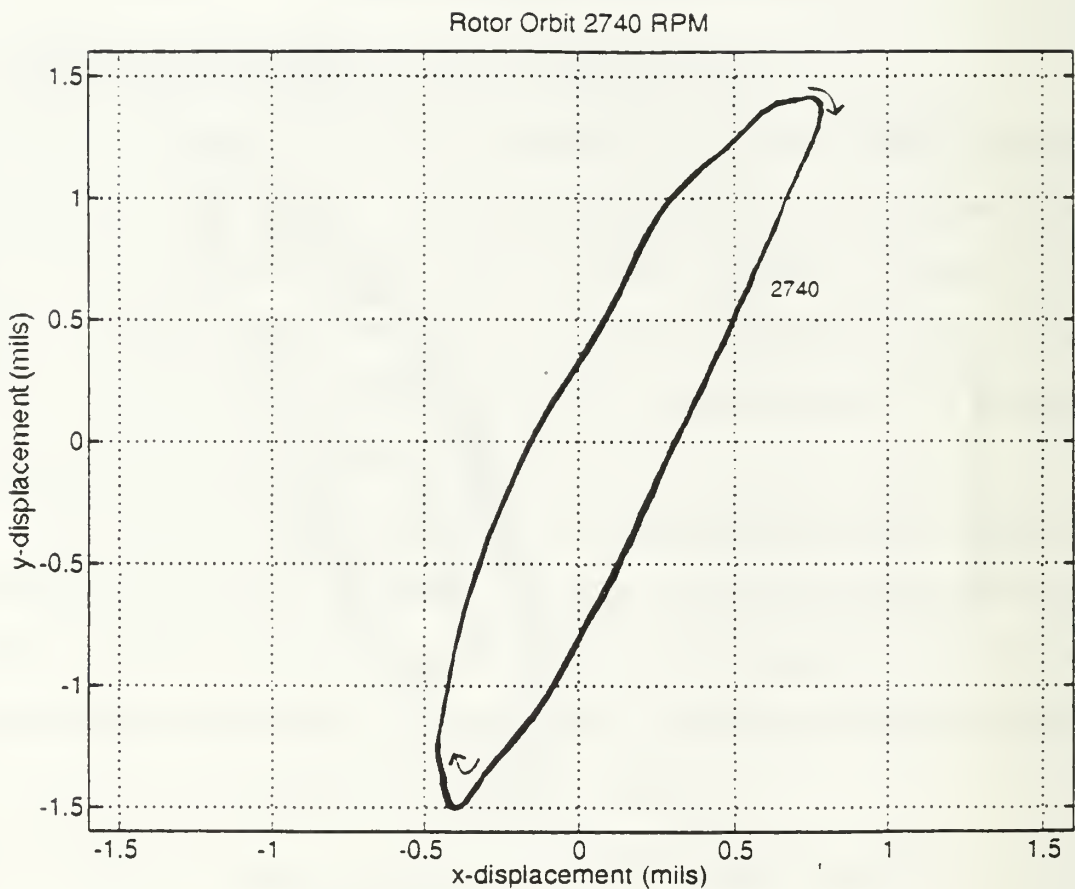


Figure 17. Rotor Orbit for the First Critical Speed 2740 RPM. The Rotor is Experiencing Forward Whirl. The Rotor Assembly is in a Simply Supported, Single Disk Configuration, Rotor Length of 14.5 Inches, Disk Located 7.25 Inches from the Inboard Bearing Support (Centered) with a 1.6 Gram Mass Imbalance.

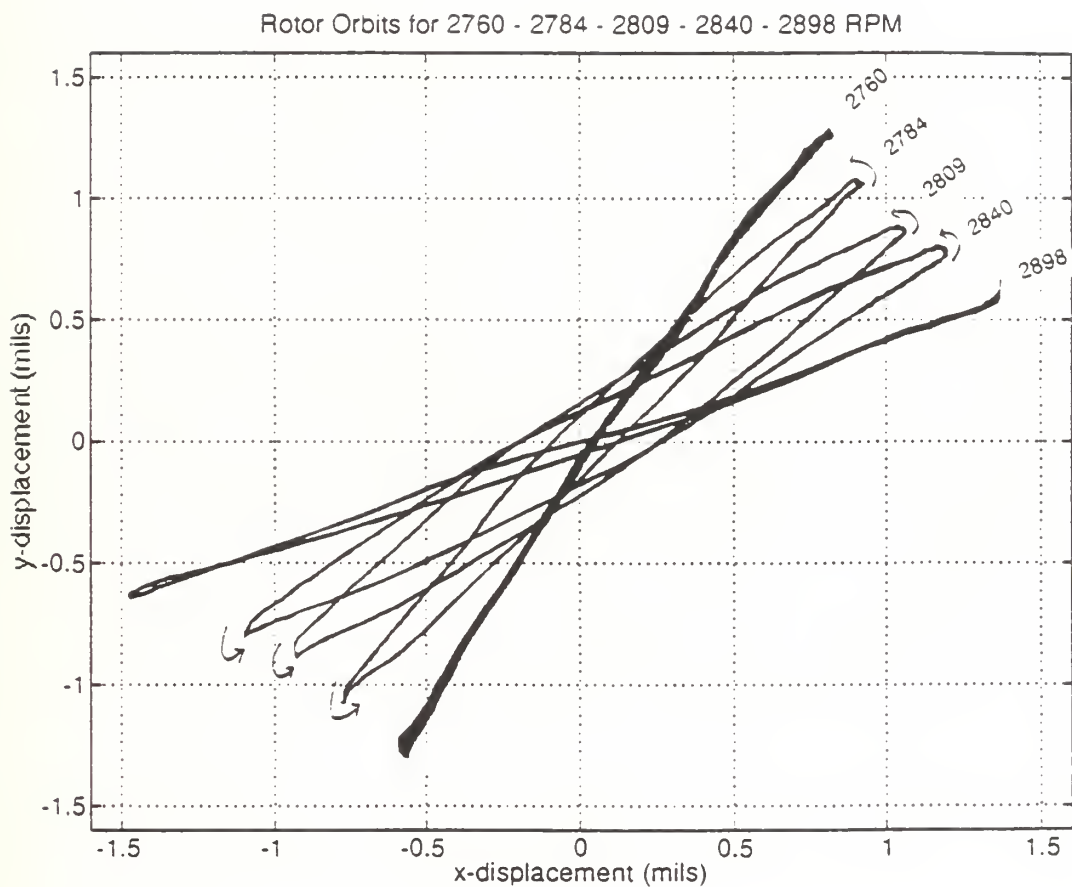


Figure 18. Rotor Orbits for Supercritical Speeds of 2760 - 2784 - 2809 - 2840 - 2898 RPM. The Rotor is Experiencing Backward Whirl. The Rotor Assembly is in a Simply Supported, Single Disk Configuration, Rotor Length of 14.5 Inches, Disk Located 7.25 Inches from the Inboard Bearing Support (Centered) with a 1.6 Gram Mass Imbalance.

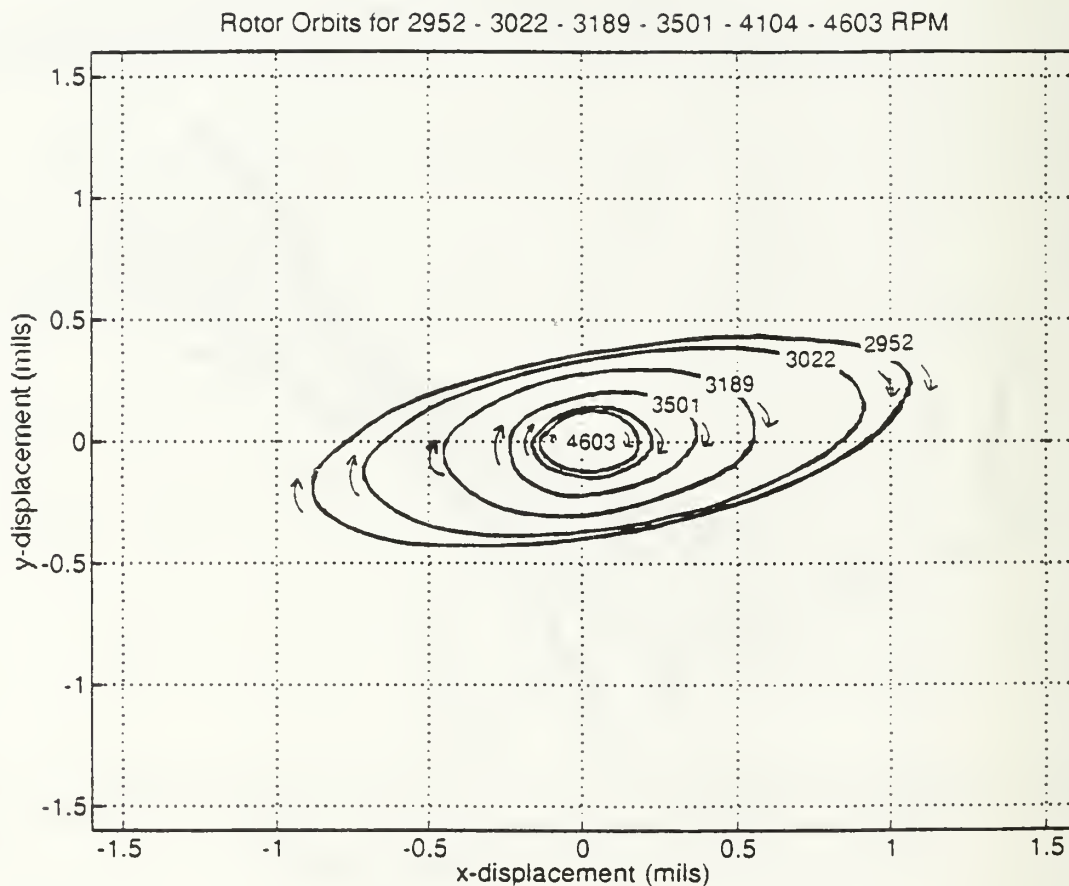


Figure 19. Rotor Orbits for Supercritical Speeds of 2952 - 3022 - 3189 - 3501 - 4104 - 4603 RPM. The Rotor is Experiencing Forward Whirl. The Rotor Assembly is in a Simply Supported, Single Disk Configuration, Rotor Length of 14.5 Inches, Disk Located 7.25 Inches from the Inboard Bearing Support (Centered) with a 1.6 Gram Mass Imbalance.

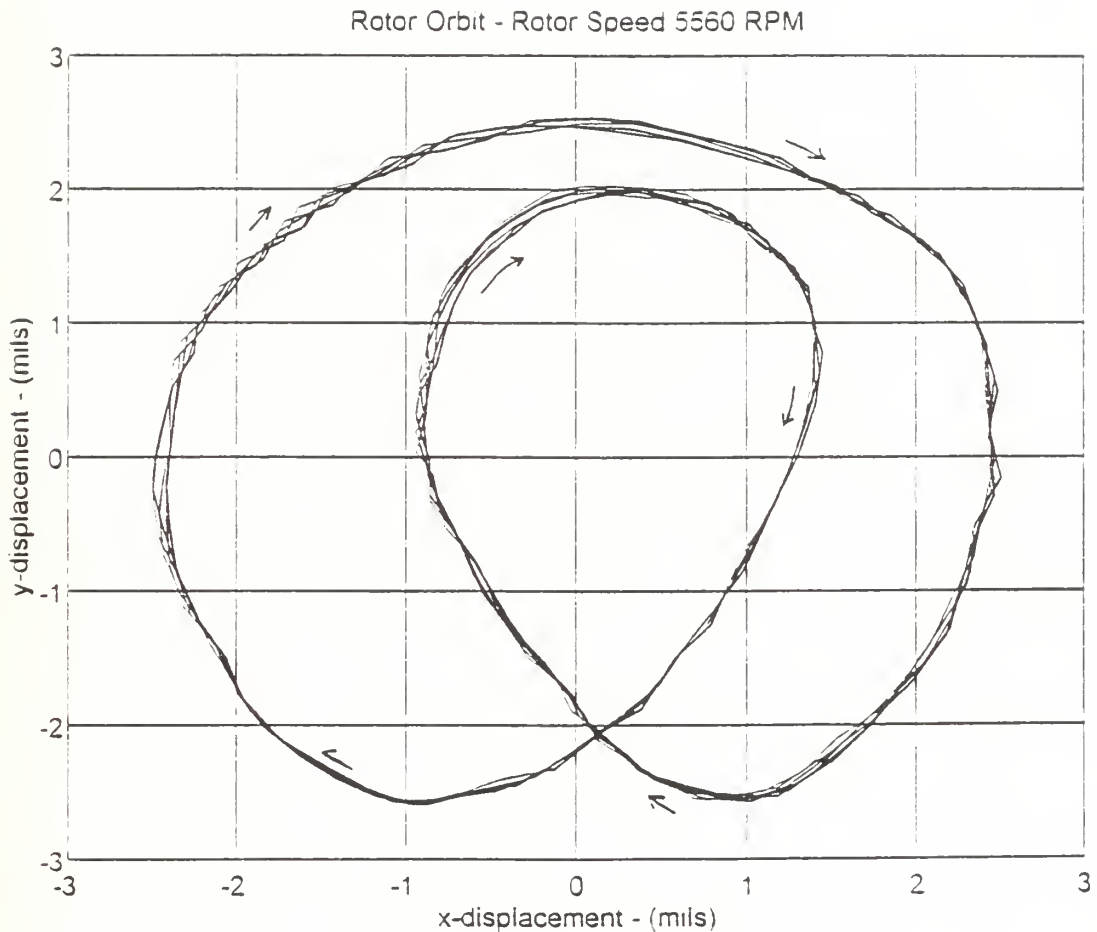


Figure 20. Rotor Orbit for Supercritical Speed of 5560 RPM. The Rotor is Experiencing Synchronous and Subsynchronous Forward Whirl. The Rotor Assembly is in a Simply Supported, Single Disk Configuration, Rotor Length of 14.5 Inches, Disk Located 7.25 Inches from the Inboard Bearing Support (Centered) with a 1.6 Gram Mass Imbalance.

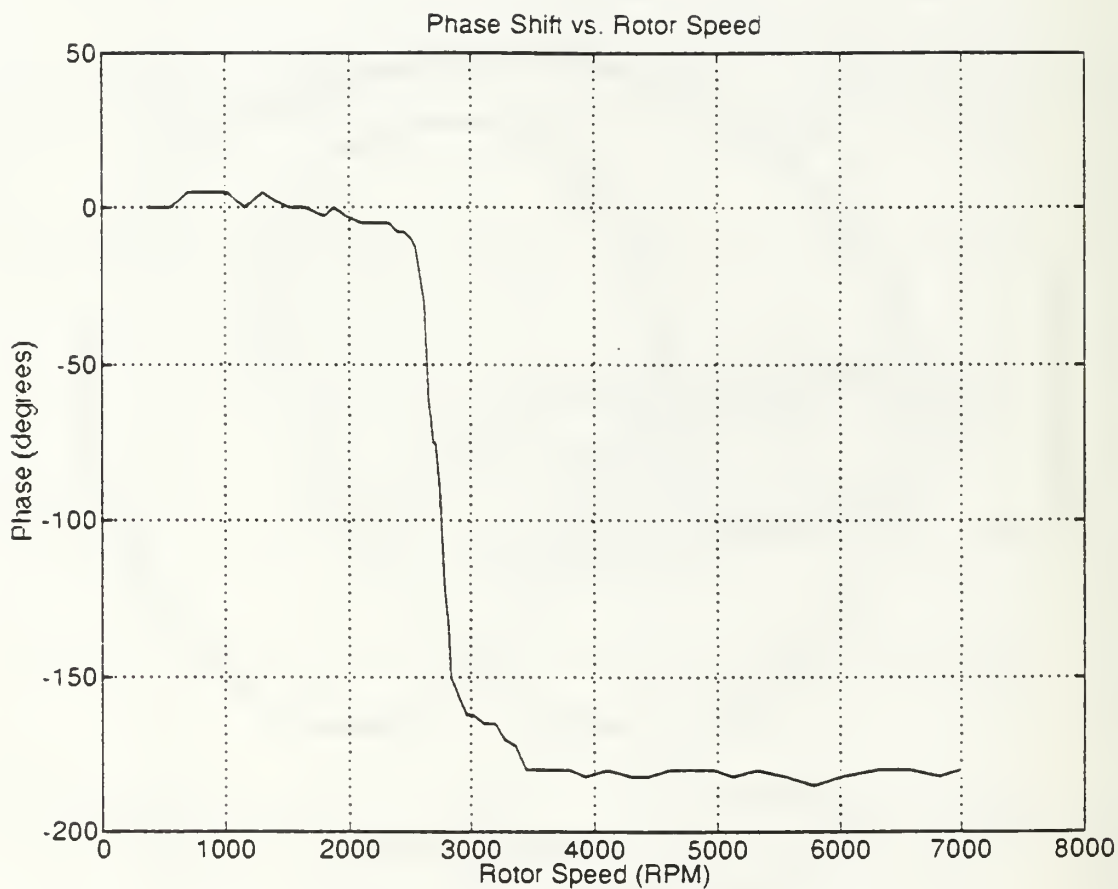


Figure 21. Maximum Y-Displacement - Mass Imbalance Phase Shift Versus Rotor Speed. The Rotor Assembly is in a Simply Supported, Single Disk Configuration, Rotor Length of 14.5 Inches, Disk Located 7.25 Inches from the Inboard Bearing Support (Centered) with a 1.6 Gram Mass Imbalance.

VI. CONCLUSIONS AND RECOMMENDATIONS

A. CONCLUSIONS

An experimental facility was developed to investigate the rotordynamic phenomena of rotating machinery. The facility consists of a Bentley Nevada Corporation Rotor Kit with a computerized data acquisition and control process. A LabVIEW Virtual Instrument was designed to control the data acquisition of the rotor position and rotor displacements. Experiments conducted included construction of Cascade plots, analytic prediction of the first lateral natural frequency while varying rotor disk placement and demonstration of a synchronous whirl condition during which backward whirl was experienced.

As seen from the results of the various experiments conducted, it can be concluded that the experimental facility can effectively demonstrate fundamental rotordynamic phenomena during subcritical, resonant and supercritical operation and serves as test for such. The experimental facility allows for the determination of the rotordynamic characteristics associated with various rotor configurations, as well as, the observation and analysis of unique rotordynamic phenomena as configuration parameters are changed.

The Nevada Bentley Rotor Kit is a versatile assembly and can easily be configured to model many phenomena that occur in rotating machinery. The flexibility of LabVIEW's virtual instruments allow for precise data acquisition control that can easily be applied to each rotor assembly configuration. The ability to collect, process and store data, enabling detailed analysis, has been demonstrated.

In summary, in consideration of the experiments conducted and the analysis of the data, it can be concluded that the experimental facility can be utilized to enhance rotordynamic research, as well as, serve as a valuable educational tool. Utilizing an model of a rotordynamic system that effectively duplicates the rotordynamic phenomena of its

larger actual system, allows for easier, more cost effective rotordynamic analysis. This can ultimately result in the prediction, elimination and/or avoidance of undesirable, machine damaging rotordynamic phenomena

Other findings that can be drawn from the supporting experimental data are directed at the rotordynamic characteristics of the simply supported, single disk rotor configuration utilized for each experiment. In particular, the facility demonstrated:

1. The construction of Cascade plots allow for the determination of general fundamental rotor characteristics and the rotordynamic phenomena experienced during subcritical, resonant and supercritical operation of the rotor assembly. Synchronous response and other subharmonic or superharmonic responses caused by nonlinearities can be detected, observed and analyzed from this plots.

2. The rotor assembly can be modeled as a pinned-pinned connection when the rotor disk is located near the center of the shaft. The experimental first lateral natural frequency can be analytically bounded using Rayleigh's Energy Method for the upper bound and Dunkerley's method for the lower bound when configured in this way.

3. A pinned-pinned analytical model of the rotor assembly is not valid when the rotor disk is located near the bearing supports. The stiffness effects of the bearing supports must be accounted for in modeling. Additionally, the stiffness properties differ for each bearing support.

4. The unique rotordynamic phenomena of backward whirl was demonstrated during the synchronous whirl experiment. Cause of this phenomena was not investigated but was assumed to be caused by the cross-coupled or asymmetric properties of the bearings. This could be attributed to oil soaking of the outboard bearing in standard automobile grade lubricating oil prior to running the experiment. Additionally, the effects of a mass imbalance can easily be seen in this experiment, thereby, reinforcing the importance of machine balancing.

5. The rotor assembly experienced oil whirl and oil whip conditions. This is evident in both the cascade plots and the synchronous whirl experiment. It should be noted that the experimental runs for the cascade plots were conducted prior to soaking the outboard bearing in the oil and, still, the rotor assembly experienced oil whirl and oil whip.

B. RECOMMENDATIONS FOR FUTURE WORK

This research has identified several areas that warrant further studies. The most obvious is to continue to determine the rotordynamic characteristics of the Nevada Bentley Rotor Kit using different rotor assembly configuration. Examples of various rotor assembly configurations included in the kit are overhangs, oil whirl and free spinner options, double disk configurations and rub conditions.

Additionally, an important compliment to the experimental facility would be an precise analytical model of the rotor assembly. The model should not only accurately predict the natural frequencies and mode shapes of the rotor assembly for various rotor configurations but also predict the occurrence and rotor response of such rotordynamic phenomena as oil whirl, oil whip, and backward whirl. To build an effective analytical model, the bearing characteristics, as well as, other assembly components should be experimentally determined.

The fluid-structure interaction problem can be investigated experimentally in the facility. Accurately determining the properties of the Oilite bearings and the effect of oil soaking the bearings or eliminating oil whip and oil whirl conditions are just a few of the applicable topics.

Overall, the experimental facility can be effectively utilized for continued rotordynamic research, as well as, educational purposes.

APPENDIX A. LIST OF DIMENSION AND PROPERTIES

Rotor Shaft:

Material:	4140 Stainless Steel	
Modulus of Elasticity:	200 GPa	29.2(10 ⁶) psi
Length:	45.7 cm	18.0 in
Diameter	0.9525 cm	0.375 in
Mass	0.253 kg	0.558 lbm
Density	7766 kg/m ³	0.281 lbm/in ³

Rotor Disk:

Material:	316 Stainless Steel	
Width:	2.54 cm	1.0 in
Inner Diameter	0.9525 cm	0.375 in
Outer Diameter	1.18 cm	3.0 in
Mass	0.816 kg	1.8 lbm

APPENDIX. B PROXIMETER CALIBRATION CURVE

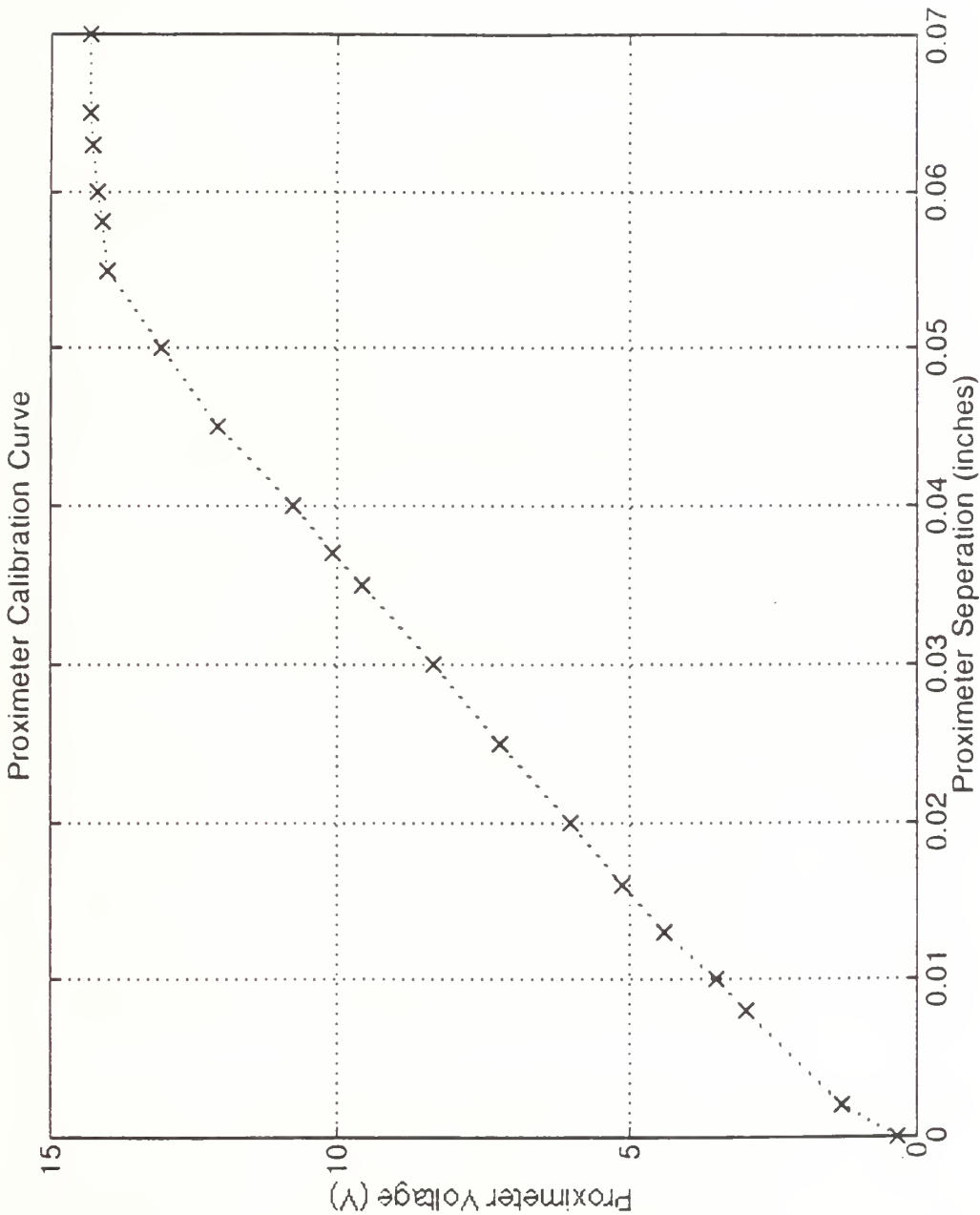


Figure 22. Eddy Current Proximeter Calibration Curve.

APPENDIX C. PROXIMETER CONFIGURATION

For all experiments conducted, the electrical connections remained the same. A listing of the electrical connections for each proximeter is found in Table II.

A. EDDY CURRENT PROXIMETERS

An X-Y probe mount was utilized for all experiments. Location of the probe mount must ensure that the vibrating rotor shaft does not contact the proximeters during operation. Prior to operation, each proximeter must be positioned with a separation distance from the rotor shaft of approximately 40 mils. This can be accomplished by disconnecting the motor power supply lead, turning the power supply on and reading between -7 and -8 volts DC at the proximeter.

Severe inference results when using an X-Y probe stand and placing the two probes in the same plane. No interference was found when using an X-Y probe stand with the two proximeters in different planes.

It should be noted that the output signal from the twelve notch disk proximeter is connected directly to speed controller and not connected to a proximeter transducer like the other proximeter outputs. This is due to the fact that the twelve notched disk provides feedback for the motor speed controller. This signal can be acquired from the proximeter (PROX) and common (COM) terminals on the back of the speed controller.

B. TTL SIGNAL CONVERTER CONNECTIONS

The TTL Signal Converter converts the single notched and 12 notched disks proximeter outputs to a TTL signal. The TTL signal converter's power supply lead (red) is connected to the +5V terminal on the SC-2070. The TTL converter's ground lead (green) is connected to the DGND terminal on the SC-2070.

TABLE II. ELECTRICAL CONFIGURATION

Proximeter Probe	Proximeter Transducer	TTL Converter	SC-2070 Channel . differential (single)
Single notched	1	white in	1 (1 - DGND) (8 - white out)
x - direction	2	n/a	2 (2 - common) (9 - output)
y - direction	3	n/a	3 (3 - common) (10 - output)
Twelve notched	n/a	black in	4 (4 - DGND) (11 - black out)

APPENDIX D. NI AT-MIO-16F-5 CONFIGURATION

Following installation of the NI AT-MIO-16F-5 multifunction I/O board and installation of the NI LabVIEW software package, software configuration of the NI AT-MIO-16F-5 was required prior to operation. LabVIEW needs the software information to recognize the NI AT-MIO-16F-5 and to set default data acquisition parameters.

Configuration is performed through the use of NI-Data Acquisition (NI-DAQ) Configuration Utility version 4.4.2. This utility is accessed through the WDAQConf icon in the LabVIEW Program Group of the Windows Program Manager window. Detailed instructions are found in [Ref. 10].

The NI AT-MIO-16F-5 is configured as shown in Table III with default data acquisition parameters listed in Table IV.

TABLE III. NI AT-MIO-16F-5 CONFIGURATION

Device	1
Base Address	0 x 220
DMA Channels	6 , 7
IRQ Level	10

TABLE IV. NI AT-MIO-16F-5 DEFAULT DATA ACQUISITION PARAMETERS

DAQ Mode	Analog Input
Polarity/Range	0 to +10 volts
Channel	Differential

APPENDIX E. ROTOR.VI VIRTUAL INSTRUMENT

A. INPUTS

With the NI AT-MIO-16f-5 Multifunction I/O board configured for differential input as discussed in Appendix D, the following is a description and listing of the front panel inputs required for execution of the VI. Default values are listed in parenthesis. See Figure 22 for a copy of the front panel.

1. CHANNELS: The analog input channels. (1, 2, 3, 4)
2. NUMBER OF SCANS (N): The number scans to acquire for each channel. (2048)
3. SCAN RATE (scans/sec): The sampling frequency, the number of scans to acquire per second. (4096)
4. INPUT LIMITS (volts): Allows data to be acquired that is outside the polarity settings of the AT-MIO-16F-5 board. The board is configured for 0-10 volts. (high limit: 15, low limit: 0).
5. TRIG CHANNEL: The channel to be used as the trigger. (1)
6. PRETRIGGER SCANS: The number of pretrigger scans to acquire. (0)
7. TRIG SLOPE: Select triggering based on a rising or falling slope. (1: rising)
8. TRIG LEVEL (volts): The triggering condition, the voltage level that must be crossed for triggering to occur. (0.8)

B. EXECUTION

To execute this VI, click on the run button on the run mode palette with the mouse. When executed, this VI starts acquiring data from the specified analog input channels into a circular buffer. The size of the buffer is determined by the VI as either 10K scans, 0.4

seconds or 2.5 times the number of scans to acquire, whichever is greatest. As data is acquired, it begins to search through the data for the trigger condition. Once the trigger condition is met, the retrieval of data begins at the inputted scan rate. The data acquisition sub-virtual instrument (SubVI), called AI Read, acquires the data in a two dimensional matrix, with the channels in columns and the scan number in rows. Data acquisition continues until the specified amount of data is obtained. The data processing portion of the VI then begins. If the trigger condition is not met within a time limit of two seconds, the VI stops the execution of the VI and displays a TIMED OUT error measure on the front panel.

The VI's block diagram and hierarchy display of the SubVI's utilized are found in Figures 23 and 24 respectively.

To obtain a print out of the front panel following execution of the VI, ensure the print mode button on the run mode palette is active prior to running the VI, click on print icon with mouse to activate. Additionally, ensure the printer is set up for Black/Gray Scale Only.

C. DATA PROCESSING, DISPLAYS AND OUTPUT PATHS

Essentially, the VI allows the data to flow two paths. One being a data processing and display path and the other an output file path .

a. Data Processing and Display Path

In the data processing and display path, the VI converts a copy of the raw data from voltage to mils for the acquired single notch, x-displacement and y-displacement data (channels 1, 2, and 3). Additionally, the VI determines and subtracts the mean for the x-displacement and y-displacement data (channels 2 and 3). This processed data is displayed on the front panel as a Rotor Orbit Plot and a Time Signal Trace.

The Rotor Orbit Plot is a graph of the y-displacement versus the x-displacement channel. Since the X-Y probe stand provides two measurements spaced 90 degrees circumferentially, rotor orbits or Lissajous patterns can be obtained. It is the path travel by the rotor during operation. Characteristics of the rotor orbit over a range of speeds can be observed from this plot. The limits for each axis are locked for this plot.

The Time Signal Trace is a voltage versus time graph for the single notched channel and the y-displacement channel. Maximum y-displacement data can be obtained by moving the y-Displacement cursor with the mouse until aligned with peaks of the y-displacement curve. Movement of the cursors can be achieved by placing the mouse directly on the cursor and dragging the mouse or by clicking on the cursor direction arrows below the plot. The values of the cursor crasher position are displayed below the plot on the cursor displays.

Additionally, phase shift between the y-displacement and single notch (mass imbalance position) traces can be obtained for each run of this VI. Selection of the y-displacement instead of the x-displacement allows for easier phase shift measurements; since the y-displacement leads the x-displacement by 90 degrees, the y-displacement begins a new cycle at the position of the single notched disk when in phase.

As seen from the front panel display, Figure 25, the single notched trace is superimposed with the twelve notched trace. This is a result of signal interference that occurs in the TTL converter. Nevertheless, this allows for increments of 30 degrees on the single notched trace.

The limits for each axis for the Signal Time Trace Plot are not locked and may be changed when necessary. This is accomplished by highlighting the desired limit to be changed with the mouse and inputting the new limit via the key board. The plot will instantaneously be replotted with the new limits when the mouse is click away from the inputted limit.

B. OUTPUT PATH

For the output file path, the VI formats a copy of the acquired *raw* data to a spreadsheet format with the first dimension (rows) being the scan number and the second dimension (columns) being the channel. This spreadsheet formatted data, channels 1 thru 4, is then sent to an user specified ASCII file.

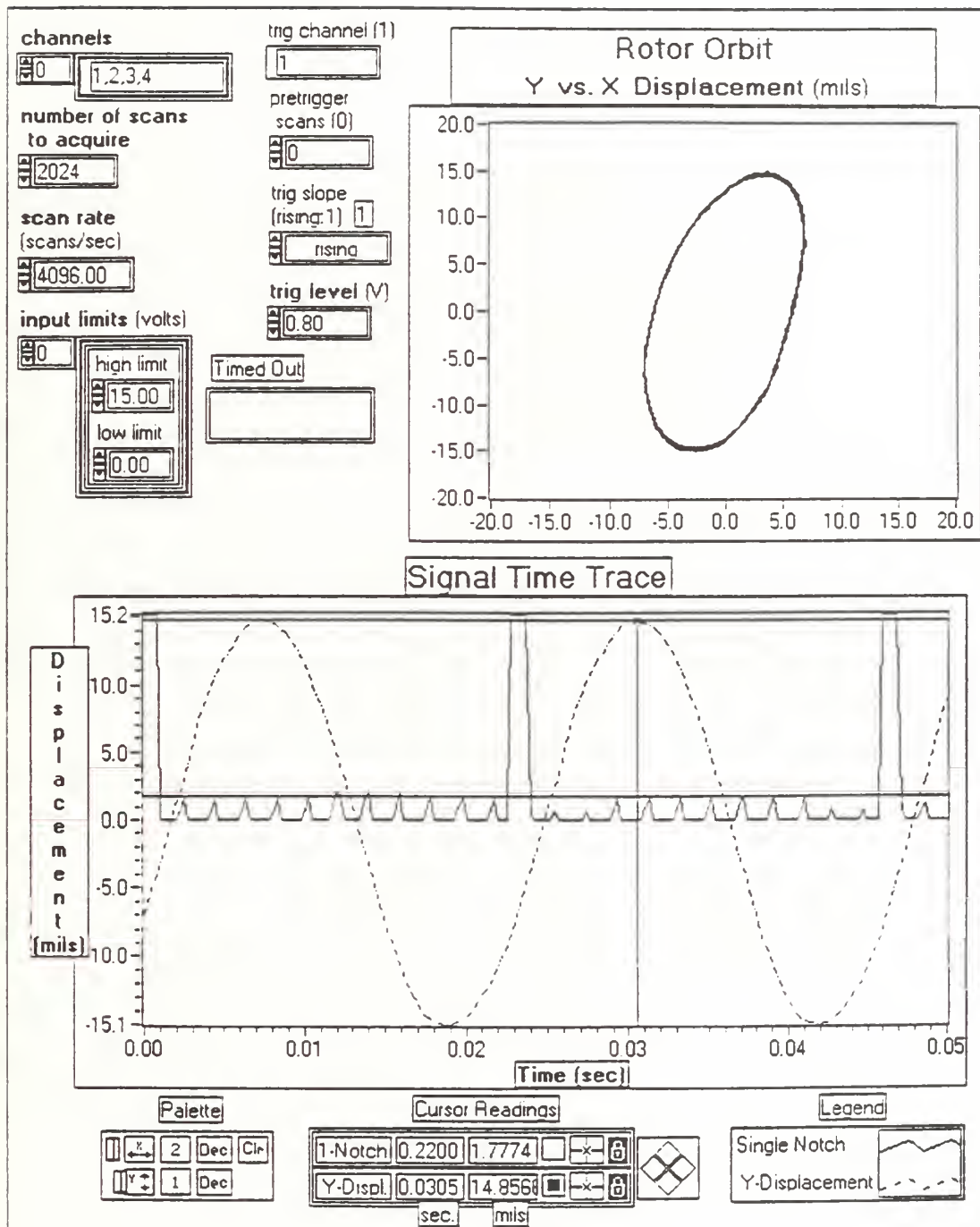


Figure 23. ROTOR.VI Front Panel.

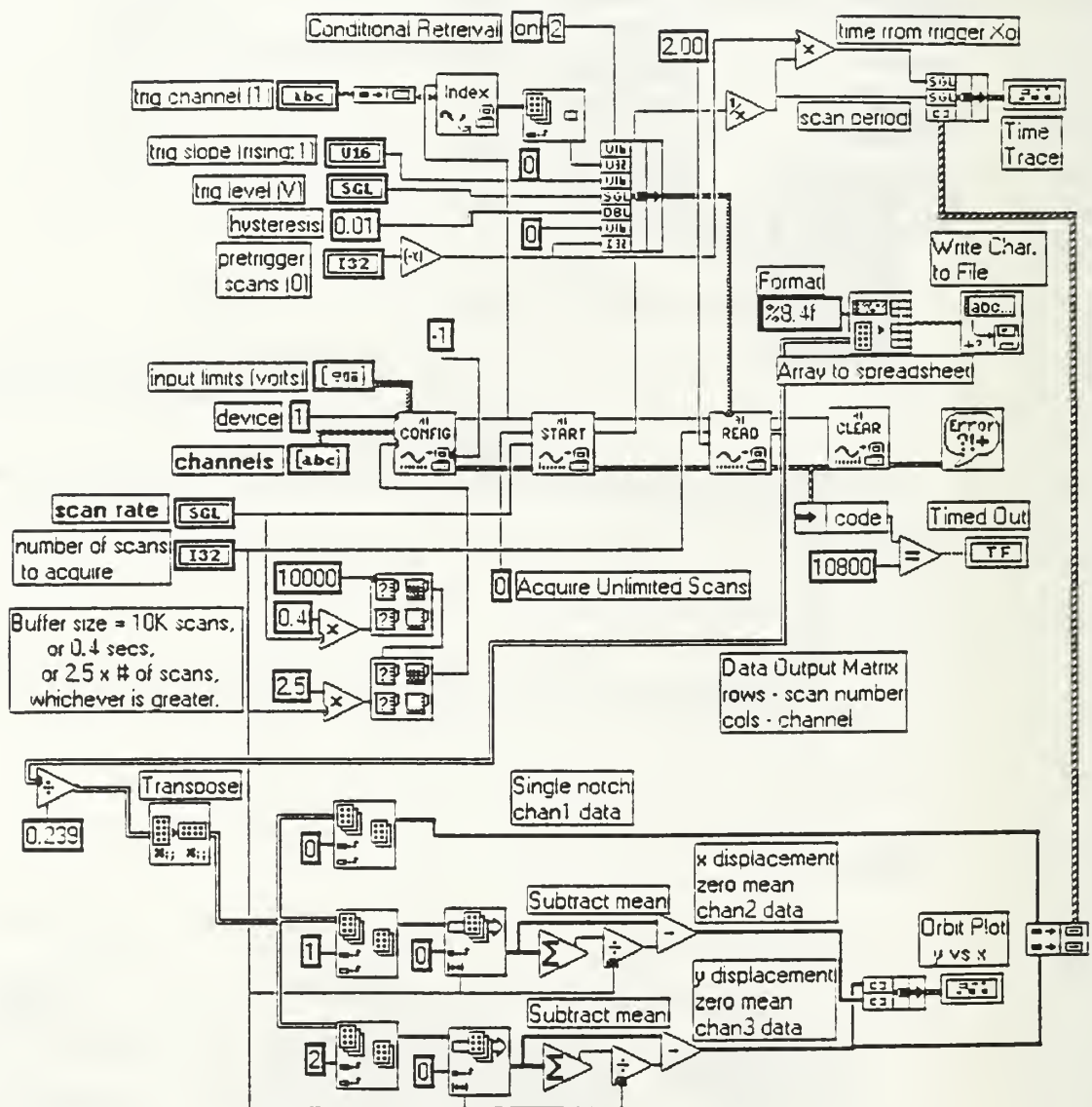


Figure 24. ROTOR.VI Block Diagram.

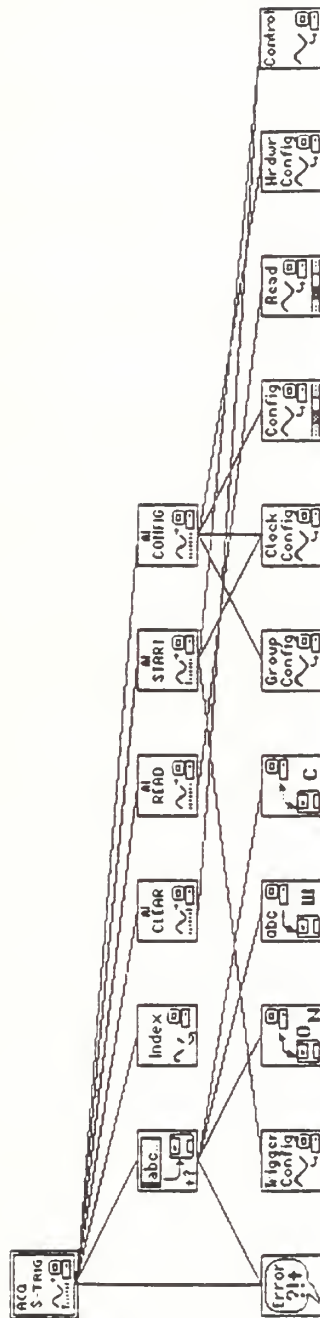


Figure 25. ROTOR.VI Hierarchy.

APPENDIX F. SYNCHRONOUS WHIRL TEST MATRIX

File Name	Rotor Speed (RPM)	File Name	Rotor Speed (RPM)
C:\LabVIEW\		C:\LabVIEW\	
MEDATA\		MEDATA\	
LAB1	380	LAB30	2809
LAB2	553	LAB31	2840
LAB3	706	LAB32	2898
LAB4	887	LAB33	2952
LAB5	1025	LAB34	3022
LAB6	1171	LAB35	3095
LAB7	1302	LAB36	3189
LAB8	1409	LAB37	3266
LAB9	1519	LAB38	3361
LAB10	1642	LAB39	3440
LAB11	1809	LAB40	3501
LAB12	1886	LAB41	3623
LAB13	1998	LAB42	3800
LAB14	2114	LAB43	3933
LAB15	2207	LAB44	4104
LAB16	2270	LAB45	4307
LAB17	2326	LAB46	4425
LAB18	2407	LAB47	4603
LAB19	2465	LAB48	4802
LAB20	2512	LAB49	4964
LAB21	2556	LAB50	5138
LAB22	2616	LAB51	5321
LAB23	2655	LAB52	5560
LAB24	2675	LAB53	5794
LAB25	2694	LAB54	6009
LAB26	2715	LAB55	6320
LAB27	2740	LAB56	6574
LAB28	2760	LAB57	6809
LAB29	2784	LAB58	7000

LIST OF REFERENCES

- [Ref. 1] National Instruments, *SC-207X User Manual*, March 1991, pp 2.1-2.15, National Instruments Corporation, 1991.
- [Ref. 2] National Instruments, *AT-MIO-16F-5 User Manual*, April 1991, National Instruments Corporation, 1991,
- [Ref. 3] James, M. L., and others, *Vibration of Mechanical and Structural Systems*, pp. 89-94, Harper & Row, Publishers, Inc., 1989.
- [Ref. 4] Thomson, W. T., *Theory of Vibrations with Applications*, p. 209, Prentice-Hall, Inc., 1972.
- [Ref. 5] Rankine, W.A., "On the Centrifugal Force of Rotating Shafts," *London Engineer*, v.27, p.249, 1869.
- [Ref. 6] Jeffcott, H. H., 'The Lateral Vibration of Loaded Shafts in the Neighborhood of a Whirling Speed - The Effect of Want of Balance,' *London Philosophical Magazine*, v. 37, pp. 304-314, 1919.
- [Ref. 7] Ehrich, F.E., *Handbook of Rotordynamics*, p 1.5, McGraw-Hill, Inc., 1992.
- [Ref. 8] Vance, J.M., *Rotordynamics of Turbomachinery*, pp. 130-131, John Wiley & Sons, 1988.
- [Ref. 9] NASA conference Publication 2409, *Instability in Rotating Machinery*, by R. Subbiah, R.B. Bhat, T.S. Sankar and J.S. Rao, pp. 145-153, 14 June 1985.
- [Ref. 10] National Instruments, *LabVIEW Users Manual*, December 1993, National Instruments Corporation, 1993.

INITIAL DISTRIBUTION LIST

	No. Copies
1. Defense Technical Information Center Cameron Station Alexandria, Virginia 22304-6145	2
2. Library, Code 052 Naval Postgraduate School Monterey, California 93943-5100	2
3. Department Chariman, Code ME Department of Mechanical Engineering Naval Postgraduate School Monterey, California 93943-5000	1
4. Professor Knox T. Millsaps Jr., Code ME/MI Department of Mechanical Engineering Naval Postgraduate School Monterey, California 93943-5000	4
5. LT Frank A. Simei Jr. 211 W. Lois Dr. Williamstown, New Jersey 08094	3
6. Curricular Officer, Code 34 Department of Mechanical Engineering Naval Postgraduate School Monterey, California 93943-5100	1
7. Naval Sea Systems Command Mr. Dan A. Groghan Director, Engines Division (SEA S6X3) Washington D.C. 20362	1
8. Bentley Nevada Corporation Mr. Don Bentley P.O. Box 157 Minden, Nevada 89423	1

DUDLEY KNOX LIBRARY
NAVAL POSTGRADUATE SCHOOL
MONTEREY CA 93943-5101

GAYLORD S

DUDLEY KNOX LIBRARY



3 2768 00307036 8